

HELM's deep: Highly extinguished low-mass galaxies seen by JWST

L. Bisigello^{1,*}, G. Gandolfi^{2,1}, A. Grazian¹, G. Rodighiero^{2,1}, G. Girardi^{1,2}, A. Renzini¹, A. Vietri², E. McGrath⁶, B. Holwerda⁹, A. Abdurro'uf^{4,5,22}, M. Castellano⁷, M. Giuliotti³, C. Gruppioni⁸, N. Hathi⁵, A. M. Koekemoer⁵, R. Lucas⁵, F. Pacucci^{10,11}, P. G. Pérez-González¹², L. Y. A. Yung⁵, P. Arrabal Haro¹³, B. E. Backhaus²¹, M. Bagley^{13,14}, M. Dickinson¹⁵, S. Finkelstein^{14,16}, J. Kartaltepe¹⁷, A. Kirkpatrick²¹, C. Papovich^{18,19}, and N. Pirzkal²⁰

¹ INAF – Osservatorio Astronomico di Padova, Via dell'Osservatorio 5, 35122 Padova, Italy

² Dipartimento di Fisica e Astronomia "G. Galilei", Università di Padova, Via Marzolo 8, 35131 Padova, Italy

³ INAF, Istituto di Radioastronomia, Via Piero Gobetti 101, 40129 Bologna, Italy

⁴ Department of Physics and Astronomy, Colby College, Waterville, ME 04901, USA

⁵ Department of Physics and Astronomy, The Johns Hopkins University, 3400 N Charles St., Baltimore, MD 21218, USA

⁶ INAF – Osservatorio Astronomico di Roma, Via di Frascati 33, 00078 Monte Porzio Catone, Italy

⁷ Space Telescope Science Institute (STScI), 3700 San Martin Drive, Baltimore, MD 21218, USA

⁸ INAF – Osservatorio di Astrofisica e Scienza dello Spazio, Via Gobetti 93/3, 40129 Bologna, Italy

⁹ Physics & Astronomy Department, University of Louisville, 40292 KY Louisville, USA

¹⁰ Center for Astrophysics | Harvard & Smithsonian, 60 Garden St, Cambridge, MA 02138, USA

¹¹ Black Hole Initiative, Harvard University, 20 Garden St, Cambridge, MA 02138, USA

¹² Centro de Astrobiología (CAB), CSIC-INTA, Ctra. de Ajalvir km 4, Torrejón de Ardoz E-28850 Madrid, Spain

¹³ Astrophysics Science Division, NASA Goddard Space Flight Center, 8800 Greenbelt Rd, Greenbelt, MD 20771, USA

¹⁴ Department of Astronomy, The University of Texas at Austin, Austin, TX, USA

¹⁵ NSF's National Optical-Infrared Astronomy Research Laboratory, 950 N. Cherry Ave., Tucson, AZ 85719, USA

¹⁶ Cosmic Frontier Center, The University of Texas at Austin, Austin, TX, USA

¹⁷ Laboratory for Multiwavelength Astrophysics, School of Physics and Astronomy, Rochester Institute of Technology, 84 Lomb Memorial Drive, Rochester, NY 14623, USA

¹⁸ Department of Physics and Astronomy, Texas A&M University, College Station, TX 77843-4242, USA

¹⁹ George P. and Cynthia Woods Mitchell Institute for Fundamental Physics and Astronomy, Texas A&M University, College Station, TX 77843-4242, USA

²⁰ ESA/AURA Space Telescope Science Institute, USA

²¹ Department of Physics and Astronomy, University of Kansas, Lawrence, KS 66045, USA

²² Department of Astronomy, Indiana University, 727 East Third Street, Bloomington, IN 47405, USA

Received 19 August 2025 / Accepted 15 December 2025

ABSTRACT

The dust content of star-forming galaxies is generally positively correlated with their stellar mass. However, some recent *James Webb* Space Telescope (JWST) studies have shown the existence of a population of dwarf galaxies with an unexpectedly large dust attenuation. Using Cosmic Evolution Early Release Science Survey (CEERS) data, we identified a sample of 1361 highly extinguished low-mass (HELM) galaxies, defined as dwarf galaxies ($M_* \leq 10^{8.5}$) with $A_V > 1$ mag or more massive galaxies with an exceptionally high dust attenuation given their stellar mass (i.e. $A_V > 1.6 \log_{10}(M_*/M_\odot) - 12.6$). The selection was performed using the multi-parameter distribution obtained through a comprehensive spectral energy distribution fitting analysis, based on optical to near-infrared data. After the exclusion of possible contaminants, such as brown dwarfs, little red dots, and high- z ($z > 8.5$) and ultra-high- z ($z > 15$) galaxies, the sample mainly includes sources at $z < 1$, with a tail extending up to $z = 7.2$. The sample has a median stellar mass of $10^7 M_\odot$ and a median dust attenuation of $A_V = 2$ mag. We analysed the morphology, environment, and star formation rate of these sources to investigate the reason behind their large dust attenuation. In particular, HELM sources have sizes (effective radii, R_e) similar to non-dusty dwarf galaxies and no correlation is visible between the axis ratios (b/a) and the dust attenuation. These findings indicate that it is unlikely that the large dust attenuation is due to projection effects, but a prolate or disc-on oblate geometry is still possible, at least for a sub-sample of the sources. We have found that the distribution of HELM sources is slightly skewed towards more clustered environments than non-dusty dwarfs and tends to be slightly less star-forming. This finding, if confirmed by spectroscopic follow-up, indicates that HELM sources could be going through some environmental processes, such as galaxy interactions.

Key words. galaxies: dwarf – galaxies: peculiar

1. Introduction

Dust is a key and ubiquitous component of the interstellar medium (ISM), despite accounting for only $\sim 1\%$ of its total

mass (see [Draine 2003](#)). Indeed, it is central to the formation and cooling of the molecular gas, and therefore to the formation of new stars. Moreover, dust profoundly impacts our understanding of galaxy evolution, given that it absorbs ultraviolet (UV) and optical radiation coming from stars re-emitting it at

* Corresponding author: laura.bisigello@inaf.it

infrared (IR) wavelengths, impacting the observed spectra and the derived physical properties. Therefore, the dust content and its evolution with cosmic time remain a key topic in extragalactic astrophysics.

Dusty galaxies have been extensively studied from the local Universe to the early cosmic epochs, showing that these systems seem to dominate the cosmic star formation budget at least out to $z = 4 - 5$ (Zavala et al. 2017; Magnelli et al. 2024; Traina et al. 2026). The existence and importance of deeply obscured objects, which are extremely faint or completely undetected in the rest-frame optical and UV, have been pointed out by several studies (e.g. Simpson et al. 2014; Franco et al. 2018; Wang et al. 2019; Talia et al. 2021; Gruppioni et al. 2020; Fudamoto et al. 2021; Enia et al. 2022; Gentile et al. 2024). In recent years, the launch of the *James Webb Space Telescope* (JWST) has allowed observations of the stellar continuum of these objects in the near-IR to deeply investigate their physical properties. Before its advent, the majority of dusty galaxies were massive and luminous systems, but their stellar continuum was poorly known or impossible to study as only far-IR or radio observations were available for these objects. Now, with JWST, we are not only investigating the stellar continuum of the brightest dusty galaxies but also pushing back their redshift and stellar mass frontiers (e.g. Pérez-González et al. 2023; Rodighiero et al. 2023; Williams et al. 2024; Gentile et al. 2025).

It has been observed that the dust attenuation (A_V) of star-forming galaxies has a positive correlation with stellar mass. On the one hand, more massive star-forming galaxies are generally dustier and are dominated by sources detected in the mid-IR (e.g. *Spitzer*; Pérez-González et al. 2005, 2008) and far-IR (*Herschel*; Rodighiero et al. 2010; Barro et al. 2019; Mérida et al. 2023). On the other hand, low-mass star-forming galaxies (with $M_* < 10^{8.5} M_\odot$) have a negligible dust content (Pannella et al. 2015; McLure et al. 2018; Shapley et al. 2023; Liu et al. 2024). This relation is shaped by the many complex mechanisms responsible for the creation and destruction of dust (see Draine 2009; Salim & Narayanan 2020; Schneider & Maiolino 2024). First, dust is produced by mass loss from asymptotic giant branch stars and supernova ejecta (e.g. Gall et al. 2011; Sarangi et al. 2018). Therefore, the correlation between dust attenuation and stellar mass can be seen as a by-product of the correlation observed between stellar mass and the star formation rate (SFR; Brinchmann et al. 2004; Noeske et al. 2007). At the same time, dust in low-mass systems can be reduced due to stellar feedback-driven outflows, which can easily expel metal-enriched gas given their low gravitational potential (Dayal et al. 2013). Moreover, it has been argued that supernova explosions could heat up the surrounding gas, reducing the amount of condensed dust (Nozawa et al. 2011; Bocchio et al. 2016; Bianchi & Schneider 2007). Finally, dust can also grow directly around ISM metals, with the growth depending on the local gas density, temperature, and elemental abundance (Draine 1990; Mancini et al. 2015; Schneider et al. 2016; Popping et al. 2017; Graziani et al. 2020).

All these phenomena that play a role in the formation of dust indicate a positive correlation between stellar mass and dust content and, as a consequence, dust attenuation. However, given the complexity and timescale of these mechanisms, we can also expect to observe galaxies deviating from such a relation. Indeed, Rodighiero et al. (2023), Bisigello et al. (2023), and Gandolfi et al. (2025) have revealed an unexpected population of low-mass galaxies with $M_* < 10^{8.5} M_\odot$ and a non-negligible dust attenuation ($A_V > 1$) mainly, but not only, located at $z < 2$, by looking for galaxies detected at $4\mu\text{m}$ but unde-

tected at $\lambda \leq 2\mu\text{m}$. This population of highly extinguished low-mass galaxies (HELM galaxies hereafter) is too faint in the optical and far-IR to be observed with past and current facilities, such as the *Hubble* (HST) or *Herschel* space telescopes, but can now be explored in the near-IR with JWST. Moreover, some HELM galaxies, being faint and red, mimic the colour expected of ultra-high redshift galaxies at $z > 15$ (Gandolfi et al. 2025; Pérez-González et al. 2025; Castellano et al. 2025), making them a poorly characterised class of interlopers when studying the extremely high- z Universe.

In this work, we take a step forwards with respect to the pioneering studies by Bisigello et al. (2023) and Rodighiero et al. (2023) to explore the nature of HELM galaxies using a larger and purer sample based on physical properties instead of colour selections. The paper is organised as follows. In Section 2 we describe the data used and sample selection. Given the faintness of HELM galaxies, we perform some preliminary analysis on the stacked photometry in Section 3, while we discuss different scenarios for the large dust attenuation of HELM galaxies in Section 4. Throughout the paper, we consider a Λ cold dark matter cosmology with $H_0 = 70 \text{ km s}^{-1} \text{ Mpc}^{-1}$, $\Omega_m = 0.30$, $\Omega_\Lambda = 0.70$, and a Chabrier initial mass function (IMF, Chabrier 2003). All magnitudes are in the AB system (Oke & Gunn 1983).

2. Data

In this work, we used data from the Cosmic Evolution Early Release Science Survey (CEERS Finkelstein et al. 2025), which covered $\sim 90 \text{ arcmin}^2$ of the Extended Groth Strip (EGS) with both spectroscopy and photometry. In particular, we considered the public release of the imaging data (v.0.6) presented in detail in Bagley et al. (2023), which include both observing epochs and six broad bands (F115W, F150W, F200W, F277W, F356W, F444W) and one medium-band Near Infrared Camera (NIR-Cam) observation (F410M). For $\sim 70\%$ of the EGS field, there are also Mid-Infrared Instrument (MIRI) data with various filter combinations. On the one hand, the CEERS programme includes sparse MIRI coverage (Yang et al. 2023), with a filter combination that may include only two deep short-wavelength filters (F560W and F770W) or six broad-band filters covering $5.6\mu\text{m}$ to $21\mu\text{m}$ with a shallower depth, depending on the pointing. On the other hand, observations from $7.7\mu\text{m}$ to $21\mu\text{m}$ are also available as part of the MIRI EGS Galaxy and AGN (MEGA Backhaus et al. 2025). However, the depths of MIRI observations are not enough to match the faintest galaxies detected with NIRCAM. Deep HST observations are also available in the entire field of CANDELS (Koekemoer et al. 2011; Grogin et al. 2011) in six filters (ACS/WFC F606W, F814W and WFC3/IR F105W, F125W, F140W, F160W) from a variety of different programmes and were all combined into mosaics at a scale of 30 mas/pixel .

Finally, we verified whether any of the sources of interest have available spectroscopic data, coming from the CEERS NIRCAM grism observations and derived using a custom extraction and contamination modelling similar to Pirzkal et al. (2018), or Near Infrared Spectrograph (NIRSpec) Multi-Object Spectroscopy observations with medium grating or the PRISM (Arrabal Haro et al., in prep.), or from the DAWN JWST Archive (DJA¹). More details are given later for specific objects.

¹ <https://dawn-cph.github.io/dja>

2.1. Photometric catalogue

This work is based on the source catalogue described by [Finkelstein et al. \(2024\)](#) and based on the NIRCcam mosaic. Briefly, short-wavelength HST and NIRCcam filter images (F606W, F814W, F115W, F150W, and F200W) were all matched to the point-spread function (PSF) of the F277W filter. At the same time, for bands with larger PSFs, such as the redder NIRCcam bands and all HST/WFC3 bands, they were corrected for missing flux using correction factors derived by convolving the F277W image to the larger PSF and measuring the flux ratio in the native image to that in the convolved image. Photometry was then performed with Source Extractor (v2.25.0 [Bertin & Arnouts 1996](#)) in two-image mode, using as the detection image the inverse-variance weighted combination of the native-resolution F277W and F356W band images. Fiducial fluxes were measured in small elliptical Kron apertures, but later corrected for missing flux (see [Finkelstein et al. 2023](#), for more details).

Given the sparsity and depth of MIRI data, we decided not to include the fiducial fluxes in the catalogue and the spectral energy distribution (SED) fitting, but to check a posteriori for the detection of single objects or in the stacked images. The final catalogue includes 101 808 sources.

2.2. SED fitting

We fitted the 13 HST and NIRCcam filter observations with the Bayesian Analysis of Galaxies for Physical Inference and Parameter ESTimation (BAGPIPES [Carnall et al. 2018](#)) code to the entire sample of 101 808 galaxies extracted in Sect. 2.1. We also included in the fit filters with non-detections – that is, $S/N < 3$ – including the measured fluxes and uncertainties directly in order to include all available photometric information without imposing strong upper limits. We added in quadrature 5% of the flux to the flux uncertainties to avoid small errors to dominate the fit and to include unknown uncertainties, such as uncertainties in SED modelling.

We considered the 2016 version of the [Bruzual & Charlot \(2003\)](#) single stellar population models with metallicity ranging from 5% solar to 2.5 times solar. As a first run, we considered a delayed star formation history (SFH) model, $\propto t e^{-(t/\tau)}$, with τ varying between 10 Myr and 10 Gyr and the age, t , ranging from 1 Myr to 15 Gyr (or the maximum age of the Universe at a given redshift, automatically included in the code). The redshift ranged from $z = 0$ to $z = 15$, with a flat uninformative prior, while stellar masses were allowed to vary between 10^6 and $10^{12.5} M_{\odot}$ considering a flat and uninformative prior. We included nebular continuum and emission lines from a pre-computed model grid considering an ionisation parameter (i.e. dimensionless ratio of densities of ionising photons to hydrogen) between $\log_{10}(U) = -4$ and -2 . Finally, for dust attenuation, we considered the reddening law by [Calzetti et al. \(2000\)](#), leaving the optical dust attenuation free to vary between 0 and 6 magnitudes. In addition, we performed an additional run that forced the dust attenuation to be below $A_V = 1$ mag.

We also performed three other runs, varying the SFH or the dust attenuation law and leaving all the other parameters unchanged. In particular, first we considered the Small Magellanic Cloud (SMC) attenuation curve ([Gordon et al. 2003](#)), varying the A_V between 0 and 6 magnitudes and keeping a delayed SFH. Second, we kept the reddening law by [Calzetti et al. \(2000\)](#) and changed the SFH to an exponentially declining one (that is, $\propto e^{-(t/\tau)}$), with τ varying between 10 Myr and 10 Gyr. Finally,

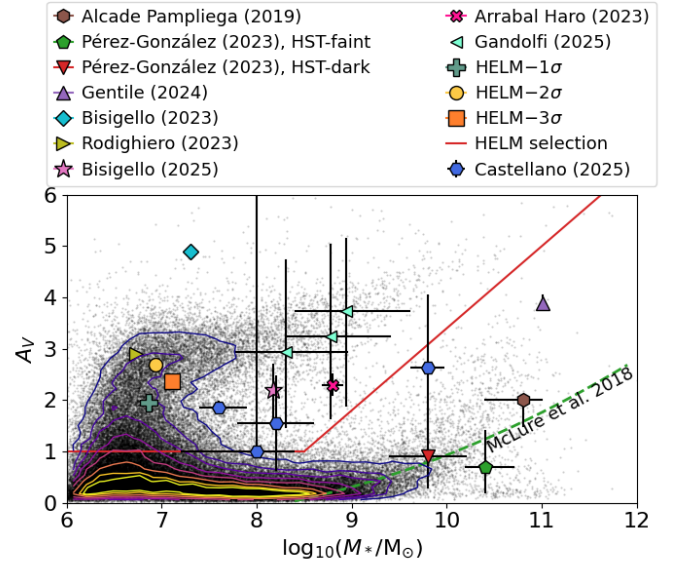


Fig. 1. Unexpected population of HELM galaxies, as visible in the stellar mass and dust attenuation plane. Black dots represent the entire CEERS sample (before any selection), derived from the first SED fitting run described in Sect. 2.2 and considering the median value of both A_V and stellar mass. Contour lines show the 20 (yellow) to 90% (dark blue) of the distribution, in steps of 10%. Coloured symbols show other samples of dusty objects from the literature ([Alcalde Pampliega et al. 2019](#); [Pérez-González et al. 2023](#); [Gentile et al. 2024](#); [Rodighiero et al. 2023](#); [Bisigello et al. 2023](#); [Gandolfi et al. 2025](#); [Castellano et al. 2025](#); [Arrabal Haro et al. 2023b](#)) and the one analysed in this paper (see Sect. 2.3). [Bisigello et al. \(2025\)](#) is a HELM galaxy confirmed spectroscopically and is also part of the HELM-2 σ sample, while the source by [Castellano et al. \(2025\)](#) has been confirmed spectroscopically but is on another field. The dashed green line shows the known relation between dust attenuation and stellar mass ([McLure et al. 2018](#)) derived at $2 < z < 3$, while the solid red line shows the selection criterion of HELM sources.

we changed the SFH to a double power law (that is, $\propto [(t/\tau)^\alpha + (t/\tau)^{-\beta}]^{-1}$), with τ varying between 10 Myr and 10 Gyr and the two power law exponents, α and β , ranging from 0.01 to 1000, with logarithmic priors.

2.3. Sample selection

From the results of the previously mentioned BAGPIPES runs, we removed objects with a bad fit (i.e. $\chi^2 > 20$, 13398 objects) and objects below the 5 σ detection limit in the F444W filter (i.e. 28.7 mag, [Finkelstein et al. 2025](#), 34795 sources). We considered the F444W for a detection given the red nature of the HELM sources. Looking at the stellar mass versus dust absorption plane for the all CEERS sample (Fig. 1), we selected HELM galaxies as objects with

$$\log_{10}(M_*/M_{\odot}) \leq 8.5 \wedge A_V > 1 \vee \quad (1)$$

$$\log_{10}(M_*/M_{\odot}) > 8.5 \wedge A_V > 1.6 \log_{10}(M_*/M_{\odot}) - 12.6,$$

using the complete multi-parameter distributions of all SED fitting runs. This selection was chosen to separate all objects with a dust attenuation above the expectation given their stellar mass. Therefore, we selected dwarf galaxies with some dust attenuation (first criterion), but also more massive galaxies with an extreme dust attenuation (second criterion).

With the above selection, we identified 3955 plausible, 203 robust, and 19 very robust HELM candidates, with 68% to 95%

Table 1. Summary of the steps considered for the sample selection.

Selection	Number of objects		
	HELM-1 σ	HELM-2 σ	HELM-3 σ
Initial HELM selection ^a	3955	203	19
Brown-dwarf ^b	3	0	0
$\chi^2(A_V < 1) < \chi^2(A_V \text{ free})$	1326	28	1
$z > 8.5$ ^c	3	1	0
Spectroscopic data ^d	9	1	1
Visual inspection	1425	15	3
Final HELM sample	1189	158	14

Notes. ^aSee Eq. (1); ^bMatching with the sample by [Holwerda et al. \(2024\)](#); ^cMatching with the sample by [Finkelstein et al. \(2024\)](#); ^dSources that are removed from the HELM sample thanks to spectroscopic data (Sect. C).

(1 σ), 95% to 99.7% (2 σ), and more than 99.7% (3 σ) of the output multi-parameter distributions within the HELM selection, respectively. In the following, we call these sub-samples HELM-1 σ , HELM-2 σ , and HELM-3 σ . These percentages were derived averaging the percentages of the four single SED fitting runs, and therefore indicate how frequent is the HELM solution among all other possibilities. For example, the minimum percentage of the multi-parameter distribution that is within the HELM selection for a single SED fitting run is 98.8% for the HELM-3 σ sample and 80% for the HELM-2 σ sample. On the other hand, one of the four SED runs could be completely outside the HELM selection for the HELM-1 σ sources, as long as the others are inside for >90%.

We cross-matched these catalogues with the sample of brown dwarfs by [Holwerda et al. \(2024\)](#), which was derived using the same dataset. We found three objects in HELM-1 σ with a probability higher than 0.7 of being a brown dwarf (see [Holwerda et al. 2024](#), or the details on the classification). We removed these brown dwarf candidates from the catalogue, reducing the sample size to 3952 objects.

We then removed objects for which the fit forcing $A_V < 1$ mag has a lower χ^2 than the run with a free-to-vary dust attenuation. For this comparison we considered the results obtained with the delayed SFH. We remind the reader that the HELM selection in Eq. 1 is based on the multi-dimensional probability distribution and not on the best point estimates. Therefore, this additional criterion verifies that the HELM solution is not only the one most represented in the multi-dimensional probability distribution, but also the one with the lowest χ^2 . With this additional criterion, we removed one object from the HELM-3 σ sample, while for all the other objects in the same sample the difference in χ^2 is $\Delta\chi^2 > 1.6$, with a median value of $\Delta\chi^2 = 6.6$. In the HELM-2 σ sample, we removed 28 objects for which the $A_V < 1$ mag solution is preferred, suggesting the possibility that their red nature is not due to reddening. Around one third of the HELM-1 σ sample has a non-dusty solution with a lower χ^2 . This is in line with the fact that these sources are the less robust HELM candidates. The HELM-1 σ sample was therefore reduced to 2626 objects.

We also cross-matched all HELM samples with the sample of $z > 8.5$ galaxy candidates by [Finkelstein et al. \(2024\)](#). There are no matches with the HELM-3 σ , while there is one with the HELM-2 σ , and three with the HELM-1 σ . On the one hand, the source in the HELM-2 σ (CEERS_90671) has a spectroscopic redshift of $z = 8.638$ [Arrabal Haro et al. \(2023a\)](#), confirming

its high- z nature. The wrong HELM identification is possibly link to the degeneracy between redshift and dust attenuation, which is strengthened by the relative faintness of this source ($F_{277W} = 28.1$ mag) and the presence of some dust attenuation, $A_V = 0.2\text{--}0.9$ ([Arrabal Haro et al. 2023a](#)). On the other hand, there is no spectroscopic confirmation of the ten candidate high- z sources in the HELM-1 σ sample. Given that our purpose is to obtain a sample as pure as possible, we decided to remove these high- z candidates from our samples anyway, but we performed further comparisons to investigate if there are any other possible high- z candidates in Sect. 4.1. In addition, there was no overlap, by construction, between the HELM samples presented here and the $z > 15$ catalogue by [Gandolfi et al. \(2025\)](#). We also verified that there was no overlap with the $z > 15$ catalogue by [Castellano et al. \(2025\)](#), as these sources had less than 20% of their multi-parameter distribution inside the HELM selection (see Section 2.3).

We also verified the availability of spectroscopic data to confirm or disclaim the HELM nature of our sources. The objects with spectroscopic data are discussed in detail in Appendix C, but the analysis allowed us to remove one object from the HELM-3 σ sample, one from the HELM-2 σ sample, and nine from the HELM-1 σ , while one HELM source from the HELM-2 σ was confirmed ([Bisigello et al. 2025](#)). The spectroscopic data were not sufficient to confirm or reject the HELM solution for the other two HELM-1 σ sources, as no evident features were observed in the spectra. We highlight that these spectroscopic follow-ups were fine tuned to high- z or massive galaxies, so an unbiased spectroscopic follow-ups of the HELM galaxies is necessary to verify the level of contamination. The spectroscopically confirmed HELM source CEERS-93316 [Arrabal Haro et al. \(2023a\)](#), which is at $z = 4.912 \pm 0.001$, was removed in our selection procedure, having $\chi^2 > 20$. In this paper we aim for a selection that is as pure as possible, at the expense of completeness.

As a final step, we visually inspected all remaining sources to remove artefacts, which are more frequent in the HELM-1 σ sample. Given that many sources are detected in only a few bands, imposing a low χ^2 does not guarantee that the source is real and without photometric issues. In Appendix B we show some examples of the objects that we removed, which include sources with strange shapes, sources at the edge of images or outside the field of view in some filters, and also cases in which no source is visible at the expected position due to issues with the extraction procedure. The final HELM samples consist of 1189 plausible sources in the HELM-1 σ , 158 robust objects in the HELM-2 σ , and 14 very robust candidates in the HELM-3 σ sample. A summary of the selection steps is reported in Table 1. The stellar mass and dust attenuation (median values of the median outputs of all SED runs) for all the HELM sources is shown in Fig. 2. Of all these sources, only two HELM-1 σ galaxies are detected in MIRI. One source, which is part of the CEERS survey ([Yang et al. 2023](#)), is detected at $12.8\ \mu\text{m}$ with a $S/N = 7.7$ and undetected at $18\ \mu\text{m}$. The other source has been observed in the MEGA survey ([Backhaus et al. 2025](#)). It has $S/N > 40$ in the $7.7\ \mu\text{m}$ filter, but is undetected ($S/N < 1$) in the other bands at $\lambda = 10, 15,$ and $21\ \mu\text{m}$. However, the first object has a suspicious annulus shape, indicating that there is probably an artefact in the F1280W image, while the second is close to the edge of the MIRI images. Therefore, neither object can be identified as a secure MIRI detection.

We also identified a control sample of low- z non-dusty dwarf galaxies to compare their physical properties with the ones of HELM galaxies to investigate the reasons of their large dust

attenuation. This control sample was selected as galaxies having a good fit (i.e. $\chi^2 < 20$), a median redshift of $z < 1$, negligible dust attenuation, $A_V < 1$, and a low stellar mass, $\log_{10}(M_*/M_\odot) \leq 8.5$, considering a confidence of 84% on the first SED fitting run (i.e. delayed SFH and Calzetti et al. (2000) reddening law). The control sample consists of 15 045 galaxies, with $A_V = 0.29 \pm 0.14$ and $\log_{10}(M_*/M_\odot) = 6.8 \pm 0.6$ on average.

2.4. Comparison between the HELM samples

In Fig. 1 we report the dust attenuation and stellar mass derived for the entire CEERS sample considering the first SED fitting run (i.e. delayed SFH, Calzetti’s reddening law) and the HELM selection criterion. From this plot, it is evident how the two-dimensional distribution shows a bimodality, with the majority of galaxies following the expected relation between stellar mass and dust attenuation, and others (forming our HELM samples) being well above the expectation. In the same figure we also report, for comparison, the median stellar mass and dust attenuation of the three HELM samples analysed in this work and other samples of dusty sources from the literature (Alcalde Pampliega et al. 2019; Pérez-González et al. 2023; Gentile et al. 2024; Rodighiero et al. 2023; Bisigello et al. 2023; Castellano et al. 2025; Arrabal Haro et al. 2023b). The first four samples were selected for being faint or dark in the optical, but bright in the near-IR or at radio frequencies and are more massive than the bulk of the HELM population. The sample presented in Bisigello et al. (2023) is generally more dust-obscured than our HELM sample. It is based on the first epoch of the CEERS survey, but it was selected for having $S/N > 3$ at $4.4 \mu\text{m}$ and $S/N < 2$ at $\lambda < 2 \mu\text{m}$. Rodighiero et al. (2023) considered a similar sample selection, but it is based on deeper data, which results in a sample with dust attenuation similar to the bulk of our HELM galaxies, but slightly less massive. The sample by Gandolfi et al. (2025) consists of three HELM candidates that, however, have some probability of being at $z > 15$. The five galaxies presented in Bisigello et al. (2025), Arrabal Haro et al. (2023b) and Castellano et al. (2025) are the only spectroscopically confirmed HELM galaxies.

We verified that there are no strong biases between the different SED fitting runs for the HELM samples (see Appendix A). The redshift and stellar mass distributions of the HELM samples are shown in Figure 3. The HELM samples present similar redshift distributions, with a median value ranging from $z = 0.29$ to $z = 0.40$. However, all galaxies in the HELM-3 σ sample are at $z \leq 0.6$, while the HELM-2 σ sample presents one source at $z > 1$, with a spectroscopic redshift of $z = 4.883$ (Bisigello et al. 2025). The HELM-1 σ sample instead extends up to $z = 7.2$. Therefore, the large majority (90%) of HELM sources are at $z < 1$. As for the stellar mass, all samples have median values between $\log_{10}(M_*/M_\odot) = 6.9$ and $\log_{10}(M_*/M_\odot) = 7.2$, but the HELM-1 σ presents a tail at $\log_{10}(M_*/M_\odot) > 8.5$ that corresponds to the galaxies at the highest redshift. We performed the two-sided Kolmogorov-Smirnov (KS) test to exclude the possibility that the HELM samples are extracted from the same distributions. We can exclude with 90% (80%) confidence that the HELM-1 σ sample is extracted from the same redshift distribution as the HELM-2 σ (HELM-3 σ) sample. We cannot exclude the possibility that the HELM-2 σ and HELM-3 σ samples are drawn from the same redshift distribution, or that any of the three HELM samples originate from the same stellar mass distribution. Given the redshift distributions of the samples, we concentrate our analysis on $z < 1$, corresponding to 1053/1189 of the

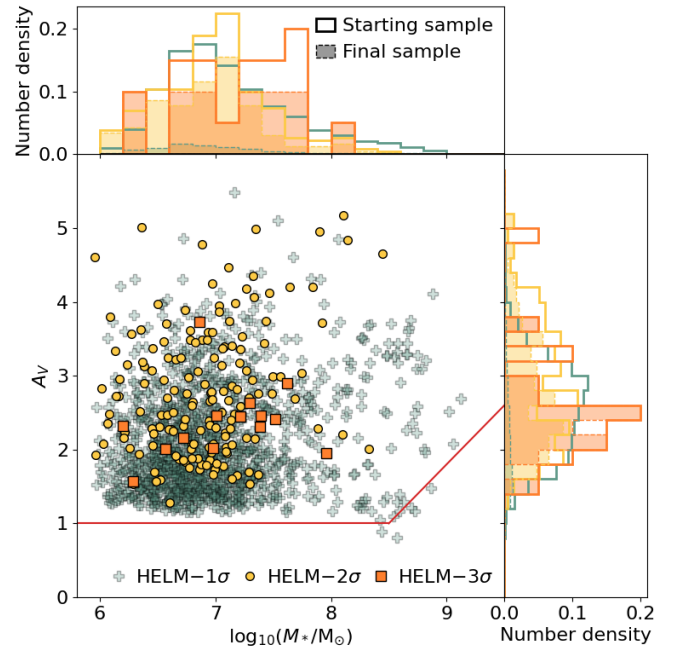


Fig. 2. Stellar mass and dust attenuation plane showing the HELM sources and the HELM selection criterion (solid red line). For the stellar mass and dust attenuation, we show the median value of the median outputs of each SED set-up. The HELM selection was performed on the multi-parameter probability distribution and not on the point estimates of the physical properties, so the median value shown here can be slightly out of the selection if one of the SED runs has a median output distant from the HELM selection. The two side panels show the number density of the HELM samples before and after the selections of Table 1.

HELM-1 σ sample, 157/158 of the HELM-2 σ sample, and all 14 objects of the HELM-3 σ sample.

It is worth noticing that HELM galaxies overall represent the minority with respect to the whole sample of observed galaxies, as they are 1.5% of the entire CEERS sample with a good SED fit. Their faint nature and their rarity, perhaps linked to a short-lived evolutionary phase, are probably the reason behind their absence in previous studies of dusty objects. They are also a minority among galaxies with a similar stellar mass and redshift (Fig. 4); therefore, their IR flux would be missed even in a stacking analysis based on stellar mass selections. Indeed, HELM sources account at maximum for fewer than 6% of all sources at $z < 1$ and with a stellar mass of around $10^7 M_\odot$, while their fraction decreases at higher stellar masses and redshifts. For example, HELM sources are $< 1\%$ of all the galaxies at $z > 1$. It is necessary, however, to consider that we did not correct for completeness and we expect the sample of HELM sources to be more incomplete than the one of non-dusty dwarfs, considering their faintness at short wavelengths.

3. Stacked photometry

As a first step, we performed a stacking analysis on the photometry of the HELM samples to verify their red nature. Indeed, the faint nature of these galaxies makes them undetected in many bands, as, on average, sources in the HELM-1 σ , HELM-2 σ , and HELM-3 σ have $S/N > 3$ in the 4.5, 6.8, and 8.8 filters, respectively, out of the 13 HST and NIRCcam bands available, but also no detections in the MIRI bands. The stack was performed in

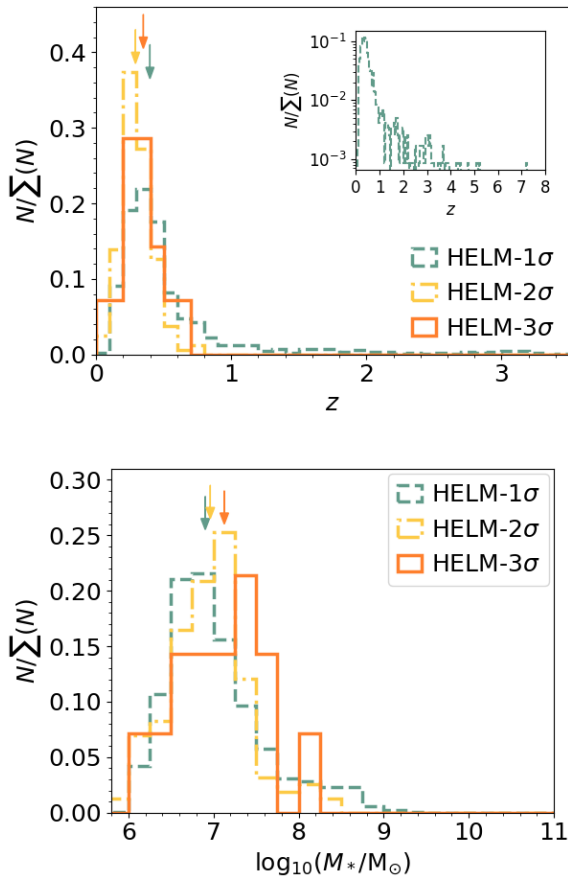


Fig. 3. Normalised redshift (top) and stellar mass (bottom) distributions of the HELM samples. Coloured arrows indicate the median of the three samples and are slightly shifted vertically for clarity. In the top panel, we limit the plot to $z < 3.5$ for visual clarity, but we show the entire range in the inset for the HELM-1 σ sample.

the rest-frame, combining all three samples and splitting them in redshift bins up to $z = 1.1$.

We started by verifying that the source is inside the observation footprint of the considered band, as it varies from filter to filter. Then, we extracted an area of $3'' \times 3''$ centred on each source. We stacked 11 objects at $z < 0.11$, 206 at $0.11 \leq z < 0.24$, 414 at $0.24 \leq z < 0.38$, 341 at $0.38 \leq z < 0.53$, 140 at $0.53 \leq z < 0.71$, 66 at $0.71 \leq z < 0.90$, and 28 at $0.90 \leq z < 1.11$. Redshift bins were chosen considering the rest-frame wavelength traced by each filter at different redshifts. The same stacking procedure was also applied to the control sample of not-dusty dwarfs.

3.1. Background removal

Before performing the stack of each object, we removed any residual local background, following the procedure presented in [Rodighiero et al. \(2023\)](#). In particular, we modelled the 1D pixel intensity distribution with the sum of a Gaussian function, whose mean corresponds to the background, and a Schechter function, which is a minor component accounting for sources within this region. The fit was performed using as initial values the maximum, the median, and 70% of standard deviation of the 1D pixel intensity distribution for the amplitude, mean, and standard deviation of the Gaussian function. For the Schechter function, we considered as initial values an amplitude of 10% the maximum

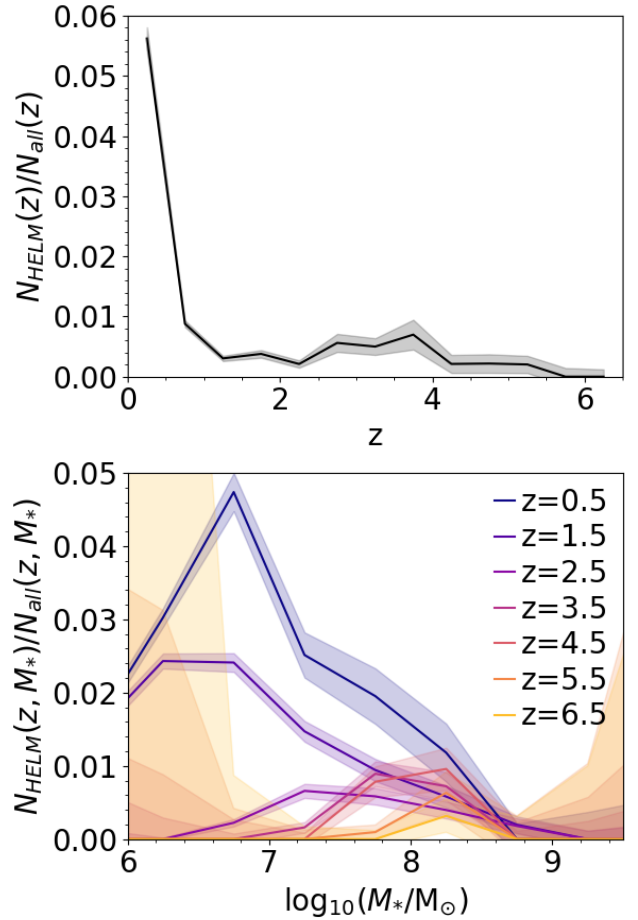


Fig. 4. Fraction of HELM sources, considering all samples, with respect to all galaxies with a similar redshift (top) and a similar redshift and stellar mass (bottom). We consider only galaxies in the entire CEERS sample with a good SED fit (i.e. $\chi^2 < 20$).

of the 1D pixel intensity distribution for the amplitude, a knee equal to the standard deviation of the 1D pixel intensity distribution, and a slope of 2. The fit is stable against reasonable changes in these initial values.

3.2. Photometric extraction and comparison

We normalised each object by its flux in the F356W filter and then we combined all images and derived the median pixel by pixel, after performing a 3σ clipping. We extracted the photometry associated with each cut-out using a $0'.3$ aperture radius, which is larger than the stacked sources. Uncertainties on the photometry were derived from the root mean square of the flux in four empty regions with a $0'.3$ aperture radius located at the corners of each stacked image.

In [Figure 5](#) we report a comparison between the photometry of the HELM sample and the control sample, all normalised to the flux observed at rest-frame $2.5 \mu\text{m}$. The coherent behaviour of both stacks support the validity of the majority of the photometric redshifts, despite the faint nature of these objects. Some discrepancies are visible in the short-wavelength slopes of each stack. However it is evident that the HELM galaxies not only have a redder continuum at $\lambda < 2 \mu\text{m}$ but also show a flatter continuum at longer wavelengths. Moreover, there is a tentative emission feature right at the position of the $3.3 \mu\text{m}$ polycyclic aromatic hydrocarbon (PAH) feature. We performed a linear fit

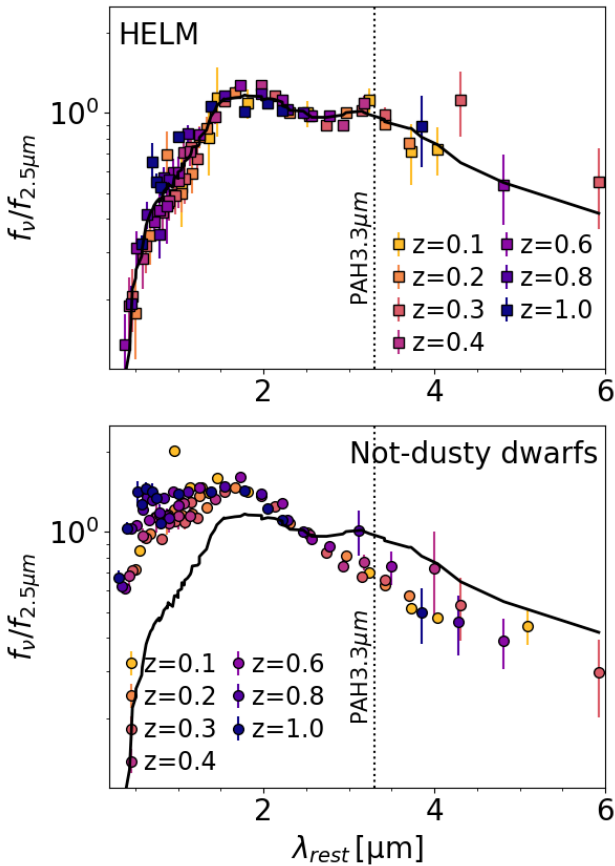


Fig. 5. Comparison between the stacked rest-frame photometry of the combined HELM samples (top) and the sample of non-dusty dwarfs (bottom) at different redshifts. Stacked photometry is normalised at $2.5\ \mu\text{m}$. We show the HELM SED (solid black lines), convolved using a top-hat function over seven data points, in both panels for comparison.

of the continuum bluewards and redwards the tentative PAH feature to derive an estimate of its equivalent width (EW). In particular, we considered the excess with respect of the continuum from $z = 0.1$ to $z = 0.3$, when the tentative feature is traced by the F356W, F410M, and F444W filters. The EW varies from $298 \pm 5\ \text{nm}$ ($z = 0.2$) to $659 \pm 6\ \text{nm}$ ($z = 0.3$). Spectroscopic follow-ups are fundamental to verify if the $3.3\ \mu\text{m}$ is indeed present and so prominent.

4. The nature of HELM galaxies

In this section we investigate some possible scenarios to explain the high dust attenuation observed in HELM galaxies. In these comparisons, except when analysing colours, we limit the analysis to objects at $z < 1$, as the limited number of sources at higher redshifts precludes the study of any redshift evolution.

4.1. Contamination by ultra-high- z galaxies

As has been highlighted by several works (e.g. [Euclid Collaboration: Bisigello et al. 2023](#); [Zavala et al. 2023](#); [Gandolfi et al. 2025](#); [Castellano et al. 2025](#)), dusty galaxies at $z < 6$ can be misinterpreted as ultra-high-redshift sources beyond $z > 15$, particularly when they are highly star-forming. To test whether this is a possibility for our HELM sources, in Fig. 6 we report the selection criteria for galaxies at $z = 15 - 20$ and $z = 20 - 30$ by [Castellano et al. \(2025\)](#). None of our sources

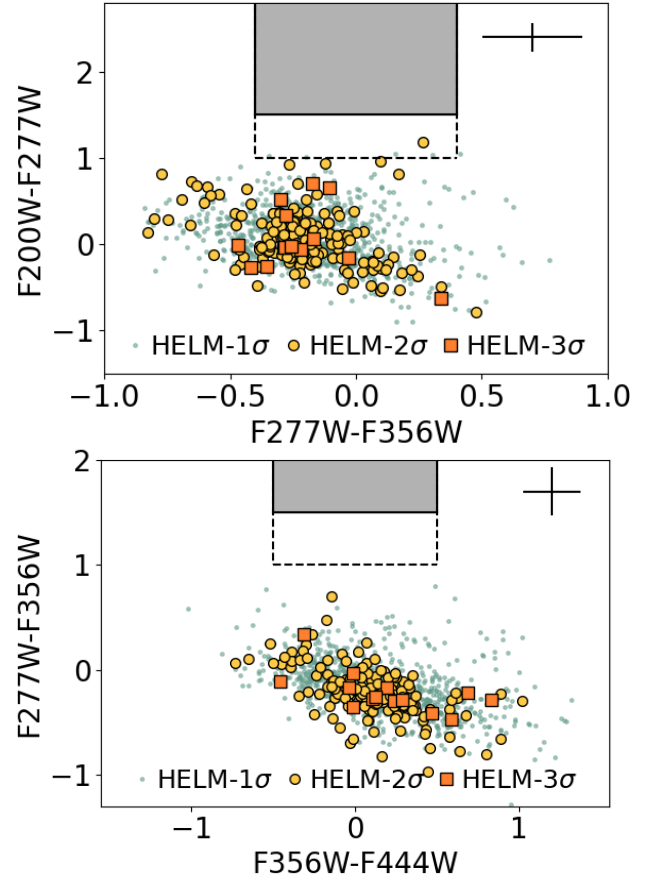


Fig. 6. Colour-colour F277W-F356W vs F200W-F277W (top) and F277W-F356W vs F356W-F444W (bottom) diagram of the HELM samples. The shaded grey area and the dashed black lines are the golden and silver selection criteria for $z = 15 - 20$ (top) and $z = 20 - 30$ (bottom) by [Castellano et al. \(2025\)](#). We show only HELM galaxies with $S/N > 3$ in the considered filters. Median errors are reported in the top right of the plot.

are inside the stricter selection criteria for $z = 15 - 20$ and $z = 20 - 30$ galaxies (shaded region), while one HELM-2 σ source and four HELM-1 σ galaxies are inside the less conservative selection (dashed black line). However, it is necessary to consider that our sources have $S/N > 2$ in bands that should be bluewards of the Lyman-break, showing that they are likely not ultra-high- z sources. One HELM-1 σ galaxy is instead at the edge of the less conservative selection criteria for $z = 20 - 30$ selection. All our HELM-3 σ sources are outside the selection criteria, but the large photometric errors could make some of our sources scatter inside the colour selection. In this regard, future spectroscopic follow-ups are fundamental to distinguish between HELM and $z > 15$ sources and further improve their selection.

From the same figure, it is evident that sources that are red in the F200W-F277W colour are blue in F277W-F356W and red in F356W-F444W (and vice versa). This behaviour is caused by the tentative $3.3\ \mu\text{m}$ PAH feature, as is visible from the stacked photometry in Fig. 5.

4.2. Contamination by passive galaxies

There is a well-known degeneracy between dust attenuation and stellar age; therefore, we investigate the possibility that we were misinterpreting passive galaxies as sources with large dust

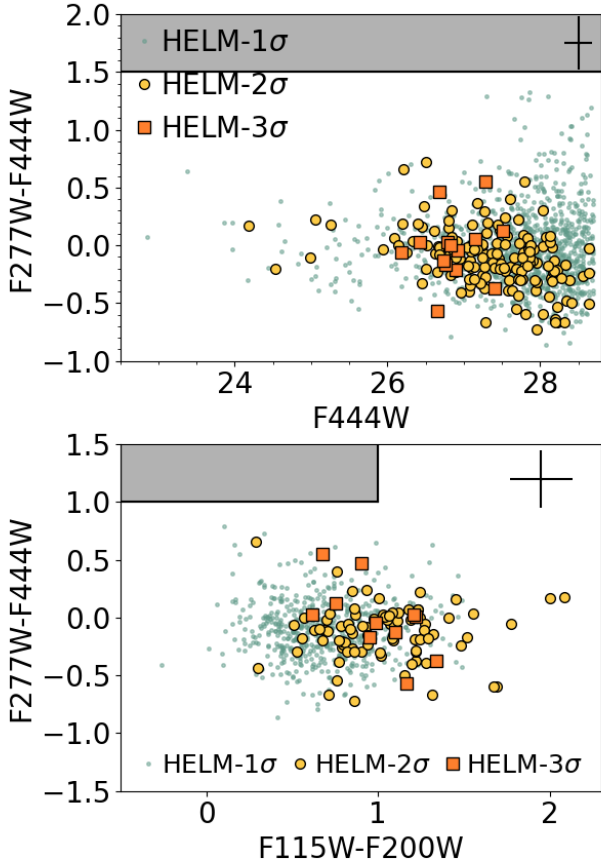


Fig. 7. Colour-magnitude $F444W-F277W$ vs $F444W$ magnitude (top) and colour-colour $F444W-F277W$ vs $F200W-F115W$ diagram (bottom) of the HELM samples. The shaded grey area is the LRD selection criteria by Barro et al. (2024, top) and by Greene et al. (2024, bottom). We show only HELM galaxies with $S/N > 3$ in the considered filters. The median errors are shown in the top right.

attenuation. To do so, we performed an additional SED fitting run whereby we forced a passive solution using BAGPIPES. In particular, we considered a burst of star formation with an age range between 1 Gyr and the age of the Universe at the fitted redshift. The remaining parameters were the same as the main run described in Section 2.2. After this run, we find that all HELM-3 σ sources, 156 out of 158 (99%) HELM-2 σ galaxies, and 1105 out of 1189 (93%) HELM-1 σ objects are still selected as HELM sources, even if they are completely passive. This suggests that these sources are too red to be described simply as passive galaxies and anyway they require a large amount of dust attenuation.

4.3. Contamination by faint little red dots?

In the past couple of years, JWST has revealed a new population of red, compact sources possibly hosting an active galactic nucleus and mainly present at $z > 4$ (e.g. Kocevski et al. 2023, 2025; Harikane et al. 2023; Matthee et al. 2024; Greene et al. 2024; Labbe et al. 2025, 2024; Killi et al. 2024; Furtak et al. 2023; Taylor et al. 2025; Durodola et al. 2025; Pérez-González et al. 2024), but with a possible sub-population extending to lower redshifts (Euclid Collaboration: Bisigello et al. 2025; Ma et al. 2025). The nature of these sources, called little red dots (LRDs), is still highly uncertain, but due to their red colour, faintness, and compactness they may partially overlap with HELM galaxies.

In particular, LRDs constitute around 1% of the population of galaxies with $M_{UV} \sim -19$ at $z \sim 5$ (see, e.g. Kocevski et al. 2025), which is similar to the percentage of HELM galaxies at lower redshift. Here we want to verify whether we are misinterpreting our sources, verifying if they could instead be the faint tail of $z > 4$ LRDs.

First, we compared our samples with the sample of LRDs identified by Kocevski et al. (2023) based on the rest-frame UV and optical slopes to identify objects with the ‘v-shape’ SED characteristic of LRDs. This sample was derived from the same CEERS dataset used in this work and we found no source in common. Second, we considered the possibility that our sources are so faint that we do not observe the blue UV rest-frame continuum, but only the red rest-frame optical one. To do so, we considered colour selections found in the literature. In particular, we compared our sample with the LRD selection criterion by Barro et al. (2024), which correspond to $F444W-F277W > 1.5$, selecting therefore objects with a red rest-frame optical slope. As is visible in Fig. 7 (top), sources in all three HELM samples occupy a completely different colour space, showing a flat or blue $F277W-F444W$ colour, which is consistent with a simple stellar continuum at $z < 1$. In the HELM-1 σ sample, there are 32 objects (2.6% of the sample) that are too faint ($S/N < 3$) in the $F277W$ filter to efficiently derive the $F277W - F444W$ colour and that could be a even fainter counterpart of the known LRDs. If we instead considered the selection criterion by Greene et al. (2024), which is based on two colour selections (i.e. $F277W-F444W$ and $F115W-F200W$), we found that no HELM sources are LRD candidates (Fig. 7, bottom).

Overall, we can exclude that any of the robust HELM sources are $z > 4$ LRDs, while a minority of the HELM-1 σ sources may be, but it highly depends on the selection criteria considered. Moreover, the overall physical properties of the HELM population seem also to exclude a direct evolution of the LRDs into the HELM.

4.4. Comparing the compactness of HELM and non-dusty dwarfs

In this section we investigate the possibility that HELM galaxies are more compact than galaxies of similar stellar mass. This would cause a large dust attenuation even if the overall dust content remained similar. To investigate this possibility, we first derived the full width at half maximum (FWHM) of both HELM galaxies and non-dusty dwarfs, fitting the radial profile of each source with a Gaussian profile using the Photutils Python package (Bradley et al. 2023). We performed the analysis with the $F277W$ filter, as non-dusty dwarfs are generally faint at longer wavelengths, while HELM galaxies are faint or undetected at shorter wavelengths. We verified, however, with smaller number statistics, that results are consistent when using the $F150W$ and the $F444W$ filters.

As can be seen in Fig. 8, the three distributions are generally similar. The median values are $0''.28$ for the non-dusty dwarfs and the HELM-1 σ sample, $0''.29$ for the HELM-2 σ sample, and $0''.30$ for the HELM-3 σ sample. We performed the one-sided and the two-sided KS test to exclude the possibility that the HELM samples are extracted from a distribution smaller than or coming from the same one as the control sample. On the one hand, the number statistics and the difference between the HELM-1 σ sample and the sample of non-dusty dwarfs are large enough that we can exclude that the distribution of the control sample is the same or larger than the HELM-1 σ sample, with a confidence above 99%. This implies that 1 σ HELM galaxies are not statistically

smaller than the non-dusty dwarfs. On the other hand, the other two HELM samples, which suffer from low number statistics, have a p value of 0.41 and 0.69 to exclude the possibility they are extracted from the same distribution of the non-dusty galaxies, and a p value of 0.20 and 0.36 to exclude that the non-dusty galaxies have a greater distribution. These results indicate that we cannot exclude that HELM-2 σ and HELM-3 σ galaxies are statistically smaller than non-dusty sources.

To validate our analysis further, we also considered the effective radius (R_e) estimated by McGrath et al. (in prep.) using GALFIT (Peng et al. 2010), converting it to a physical scale using the photometric redshift. Single-component Sérsic profiles were fitted to all sources with $F356W < 28.5$, using empirical PSFs generated by stacking isolated stars across all CEERS fields (Finkelstein et al. 2023). The magnitude cut selected all sources in the HELM-3 σ , 95% of HELM-2 σ galaxies, 81% of the HELM-1 σ sample, and 59% of the control sample of non-dusty dwarfs, considering only sources with $z < 1$. The Sérsic profile fit was reliable (flag 0 and 1) for six HELM-3 σ galaxies, 66 HELM-2 σ sources, 445 HELM-1 σ objects, and 35% of the control sample. We show the distribution of the effective radius for the three HELM samples and the control sample in Fig. 9. The median effective radius is 0.9 kpc for the non-dusty dwarfs and the HELM-1 σ sample, 1.0 kpc for the HELM-2 σ sample, and 0.5 kpc for the HELM-3 σ sample. We can exclude, using the one-sided KS test, that the HELM-1 σ and HELM-2 σ samples are extracted from a distribution smaller than the non-dusty dwarfs with a probability larger than 89%, in both cases. The statistic is too small to obtain meaningful constraints for the HELM-3 σ sample, but the hints point to these sources indeed being generally smaller. Moreover, the two-sided KS test cannot discard with a high significance the possibility that all samples are extracted from the same distribution, as the comparison with the control sample gives a p value of 0.21, 0.23, and 0.16 for the HELM-1 σ , HELM-3 σ , and HELM-3 σ samples, respectively.

Therefore, we can exclude that the large dust attenuation observed in HELM galaxies is driven by HELM galaxies being more compact than average for the HELM-1 σ sample and even for the HELM-2 σ one. The sample size is instead too small to exclude this possibility with high confidence for HELM-3 σ . These results are also limited by the spatial resolution of JWST images, as 46–50% of the sources are barely resolved, having sizes below three times the FWHM of the filter PSF.

4.5. Testing if HELM galaxies preferentially edge-on

Another possibility is that HELM galaxies are preferentially edge-on galaxies, making the large dust attenuation a result of the line of sight. To verify this possibility, we considered the axis ratio b/a , where b and a are the minor and major axis of each source, derived as part of the Sérsic profile fit mentioned in the previous section.

Figure 10 shows the distribution of the axis ratio for the HELM samples as well as the control sample. As for the sizes, we show the results using the F277W filter, as dusty dwarfs are generally undetected at shorter wavelengths. The median axis ratio of the control sample is $b/a = 0.51$, with the HELM samples having similar median values, that is $b/a = 0.47$ for the HELM-1 σ , $b/a = 0.51$ for the HELM-2 σ , and $b/a = 0.62$ for the HELM-3 σ . We verified the statistical significance of these differences using the one-sided and the two-sided KS tests, but we can only exclude that the HELM-1 σ sample is extracted from a greater or similar distribution than the control sample with a confidence of 98%. The absence of a correlation between the

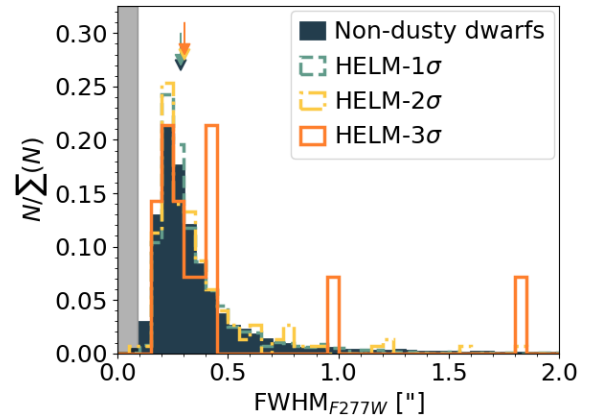


Fig. 8. Comparison between the sizes of HELM galaxies and non-dusty dwarfs. We show the distributions of the FWHM in the F277W filter for the control sample of non-dusty dwarfs (filled dark blue histogram), for the HELM-1 σ sample (dashed green histogram), for the HELM-2 σ sample (dash-dotted yellow histogram), and for the HELM-3 σ sample (solid orange histogram). All samples are limited to $z < 1$. Coloured arrows indicate the median of the three samples and are slightly shifted vertically for clarity. The shaded grey area shows the FWHM of the F277W filter PSF.

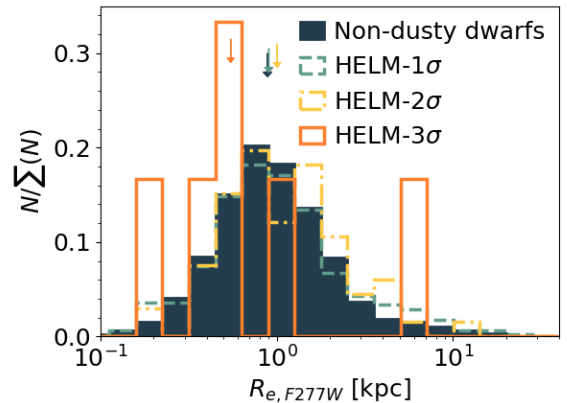


Fig. 9. Comparison between the effective radius in physical scale of HELM galaxies and non-dusty dwarfs. We show the distributions in the F277W filter for the control sample of non-dusty dwarfs (filled dark blue histogram), for the HELM-1 σ sample (dashed green histogram), for the HELM-2 σ sample (dash-dotted yellow histogram), and for the HELM-3 σ sample (solid orange histogram). All samples are limited to $z < 1$. Coloured arrows indicate the median of the three samples and are slightly shifted vertically for clarity.

dust attenuation and the axis ratio (Fig. 11) supports that the HELM galaxies are not preferentially edge-on galaxies.

Pandya et al. (2024) have shown that disc-on oblate systems preferentially have larger dust attenuation. We can exclude this possibility only for 30–40% of the HELM samples, as the derived axis ratio is larger than the one expected for disc-on oblate systems ($b/a > 0.4$). However, the same fraction of the b/a ratio is also present among the non-dusty dwarfs.

Another possibility is that these galaxies are prolate systems, with the major axis pointing towards us. Studies have shown that dry major mergers could originate prolate galaxies, but their fraction seems to also strongly decrease with decreasing stellar

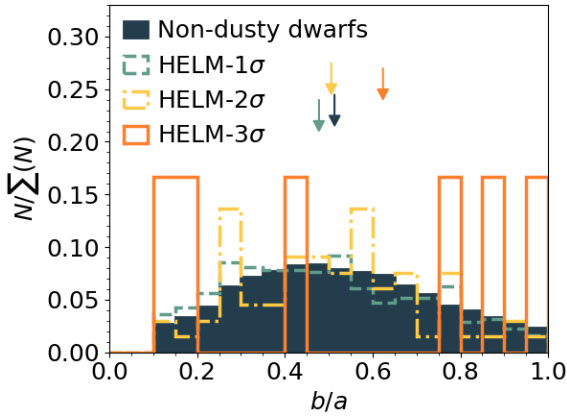


Fig. 10. Comparison between the axis ratio of HELM galaxies and non-dusty dwarfs. We show the distributions of the ellipticity in the F277W filter for the control sample of non-dusty dwarfs (filled dark blue histogram), for the HELM-1 σ sample (dashed green histogram), for the HELM-2 σ sample (dash-dotted yellow histogram), and for the HELM-3 σ sample (solid orange histogram). All samples are limited to $z < 1$. Coloured arrows indicate the median of the three samples and are slightly shifted vertically for clarity.

mass (e.g. Tsatsi et al. 2017; Li et al. 2018). There are some rare cases of dwarf spheroidal galaxies showing prolate shapes in the local Universe (e.g. Ebrova & Lokas 2015), while their fraction seems to increase with redshift. However, we cannot test these scenarios for HELM galaxies using only photometric data, due to the degeneracies when converting projected shapes into intrinsic ones and their faintness.

We can therefore conclude that with the current data it seems that an inclination effect is probably not the primary cause of the large dust attenuation observed in HELM galaxies. However, observations with a higher angular resolution are necessary to have more robust conclusions and spatially resolved spectroscopic data are necessary to investigate possible prolate shapes.

4.6. Investigating if HELM galaxies linked to galaxy interactions

A galaxy interaction could potentially increase the SFR of a galaxy, and also boost metal and dust production. Another possibility is that HELM galaxies are tidal dwarfs (e.g. Zwicky 1956; Duc & Mirabel 1999), forming from debris in interacting or merging galaxies. While these scenarios differ in many aspects, such as the absence of non-baryonic dark matter in tidal dwarfs (Lelli et al. 2015), they both require HELM galaxies to be in over-dense regions. A good estimation of the galaxy environment of HELM galaxies would require one to measure their spectroscopic redshift and the one of their neighbours over a large area. At the moment this is not available, so we estimated the projected distance of the 5th neighbour (d_{5th}) as a proxy for a galaxy environment. For this estimation, we considered all reliable galaxies in the catalogue with photometric redshifts consistent with the one of HELM galaxies, within the 1 σ uncertainties.

As is shown in Figure 12, there is little difference in the median of the four distributions, that is $d_5 = 25.7$ kpc, 27.6 kpc, 22.6 kpc, and 25.7 kpc, for the sample of non-dusty dwarfs, HELM-1 σ , HELM-2 σ , and HELM-3 σ , respectively. However, the distributions of HELM-1 σ and HELM-2 σ sources are slightly more skewed to lower d_5 . Indeed, the one-sided

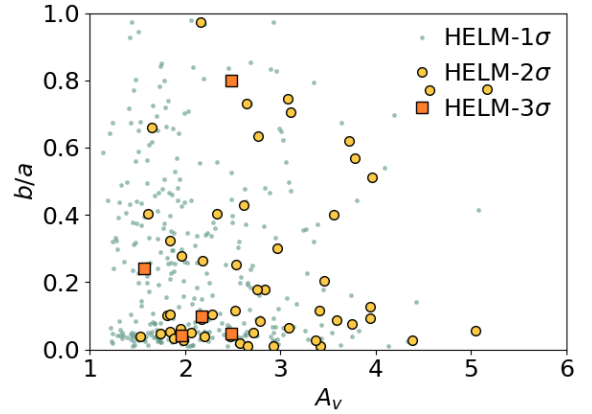


Fig. 11. Dust attenuation vs ellipticity of the HELM galaxies, as derived considering the F277W filter. There is no evidence of a correlation between the dust attenuation and the ellipticity. We limited each sample to $z < 1$.

and two-sided KS tests discarded with a confidence higher than 99.9% that the distribution of non-dusty dwarfs is smaller or the same as the ones of the HELM-1 σ and HELM-2 σ samples. Again, perhaps because of the limited statistics, we cannot draw similar conclusions for the HELM-3 σ sample.

Given the dependence of clustering on stellar mass, we more carefully verified that this discrepancy is not driven by variations in the stellar mass or redshift distributions of the non-dusty and HELM samples. For this reason, for each source in the HELM samples we selected three non-dusty dwarfs that have the minimum difference in redshift and stellar mass. The median distance of the 5th neighbour of these non-dusty dwarfs is similar to the previous ones, as they become $d_5 = 26.5$ kpc, $d_5 = 23.3$ kpc, and $d_5 = 25.7$ kpc for the sub-samples matched to the HELM-1 σ , HELM-2 σ , and HELM-3 σ samples, respectively.

Based on the results on the HELM-1 σ and HELM-2 σ samples, some HELM galaxies could be more clustered than their non-dusty counterparts. In this case, we need to understand if they are going through an interaction or if they are the product of interactions, such as tidal dwarfs (e.g. Zwicky 1956; Duc & Mirabel 1999). Dynamical studies to verify the presence or absence of a dark matter halo and spectroscopic studies to derive gas abundances are beyond the possibilities of this work and JWST’s angular resolution limits any detailed morphological study. However, we can analyse if these galaxies are going through a burst of star formation, possibly induced by galaxy interactions. Bisigello et al. (2023) have already shown, although using a selection based on colours and not on physical properties, that this scenario seems to be excluded. We confirm their finding in Fig. 13. Indeed, the median sSFR of the HELM samples is smaller than the value of the non-dusty dwarfs, being $\log_{10}(\text{sSFR}/\text{yr}^{-1}) = -9.1$ for the non-dusty dwarfs and from $\log_{10}(\text{sSFR}/\text{yr}^{-1}) = -9.6$ to $\log_{10}(\text{sSFR}/\text{yr}^{-1}) = -9.4$ for the HELM samples. The two-sided KS test shows that we can exclude with a confidence larger than 99.9% that the HELM samples are derived from the same distribution as the non-dusty dwarfs. Therefore, we can exclude that the large dust attenuation of HELM galaxies is driven by a burst of star formation. It is necessary, however, to take into account that the sSFR estimation is based on SED fitting with limited photometry, given that both the non-dusty dwarfs and the HELM galaxies are generally faint. In addition, considering the available data, the possibility

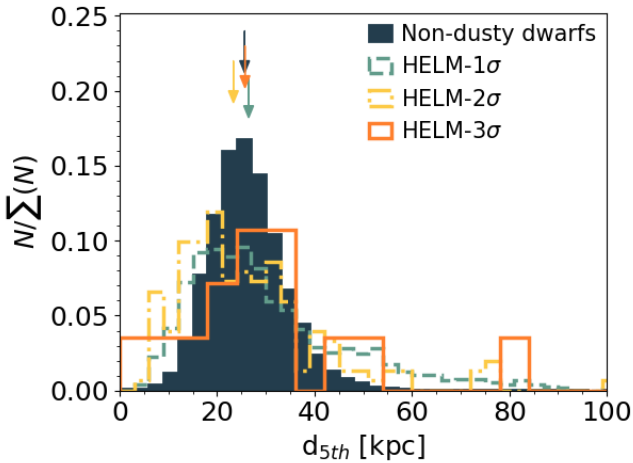


Fig. 12. Distance of the 5th neighbour, used as a proxy for galaxy clustering. We considered all sources with photometric redshift consistent with the photometric redshift of HELM galaxies, within 1σ uncertainty. We considered the photometric redshift of HELM sources to convert from an angular to a physical scale. Histograms are shown for the control sample of non-dusty dwarfs (filled dark blue histogram), for the HELM- 1σ sample (dashed green histogram), for the HELM- 2σ sample (dash-dotted yellow histogram), and for the HELM- 3σ sample (solid orange histogram). All samples are limited to $z < 1$. Coloured arrows indicate the median of the three samples and are slightly shifted vertically for clarity.

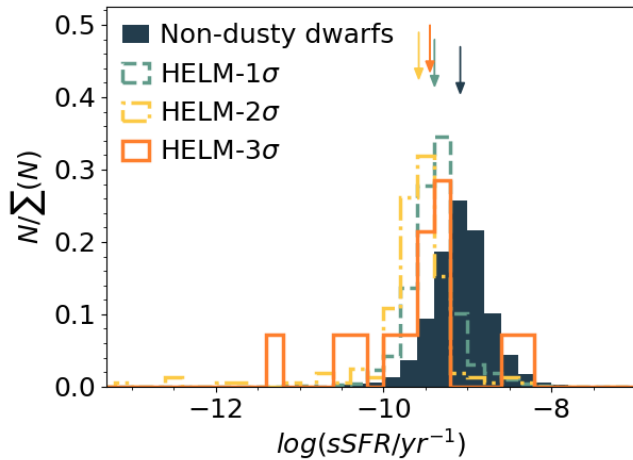


Fig. 13. HELM galaxies are generally less star-forming than their non-dusty counterparts. We show the sSFR histograms of the control sample of non-dusty dwarfs (filled dark blue histogram), of the HELM- 1σ sample (dashed green histogram), of the HELM- 2σ sample (dash-dotted yellow histogram), and of the HELM- 3σ sample (orange solid histogram). Coloured arrows indicate the median of the three samples and are slightly shifted vertically for clarity. All samples are limited to $z < 1$.

that these objects are instead post-starburst galaxies is still totally open.

5. Conclusions

Using CEERS data, we selected three classes of HELM galaxies, considering the fraction of their multi-parameter distributions

that fall within the HELM selection, derived through SED fitting and using a variety of configurations. We then cross-matched these samples with catalogues of $z > 8.5$ galaxies and brown-dwarfs to remove possible contaminants. We also removed any sources for which the SED fitting preferred a $A_V < 1$ mag solution and we visually inspected all remaining sources. We obtained 14 very robust HELM candidates (HELM- 3σ) with a probability of $>99.7\%$ of being HELM sources, 158 robust candidates (HELM- 2σ) with a probability between 95 and 99.7%, and 1189 plausible HELM galaxies (HELM- 1σ) with a probability between 68 and 95%.

The large majority (90%) of the HELM sources are at $z < 1$, indicating they are mainly a low- z population. They have a median stellar mass of $10^7 M_\odot$ and a median dust attenuation of $A_V = 2$ mag. However, the only galaxies confirmed spectroscopically are at $z > 4$. This may be due to selection biases, as these were previously identified as $z > 10$ candidates, or indicate a general failure in the SED fitting analysis to systematically derive their redshifts. Spectroscopic follow-ups are therefore pivotal to clarify the redshifts of these galaxies.

The stacked photometry of HELM sources, compared with a control sample of non-dusty dwarfs, reassured us of the red nature of these galaxies, showing also a tentative $3.3 \mu\text{m}$ PAH feature. At the same time, the use of various colour selections can exclude the possibility that the majority of these sources are bright LRDs, while we cannot exclude that they are faint ones. We can also exclude the possibility that the majority of these sources are strong candidates at $z > 15$.

Examining the morphology of HELM sources, while bearing in mind that they are faint and relatively compact, we can rule out that the inclination is a major factor contributing to the high dust attenuation observed in HELM galaxies. Moreover, the size distributions of the HELM sub-samples and the control sample do not show any statistical difference. At the same time, with the current data we cannot investigate if HELM sources are prolate systems.

The analysis of the environment shows that the distribution of HELM galaxies (HELM- 2σ and HELM- 1σ) may be slightly skewed towards denser environments, although it has a similar median to the control sample. While spectroscopic follow-ups are fundamental to confirm this statement, this may indicate that HELM galaxies are the result of galaxy interactions (e.g. tidal dwarfs, stripped galaxies, merger-triggered starbursts). However, there seems to be no indication of a burst of star formation, as HELM sources are on average less star-forming than non-dusty dwarfs, but there is still the possibility that they are post-starburst galaxies.

HELM galaxies represent only 1.3% of the entire CEERS sample and at maximum 5% of the galaxies with a similar redshift and stellar mass. Therefore, they could also represent a short-lived evolutionary phase: AGB stars may have saturated these galaxies with carbon-based dust, while not enough supernovae have gone off to blow all the dust out, or at least to create enough holes in it.

To conduct a more in-depth analysis of the morphology of HELM galaxies and unveil any possible signature of galaxy interactions we need to wait for the upcoming Extremely Large Telescope (ELT), which will have a PSF ≈ 6 times sharper than that of JWST. At the same time, to verify that dust attenuation is not purely a geometrical effect, it will be necessary to observe these galaxies in the far-IR to trace their dust continuum. HELM sources are expected to be too faint to be observable with the Northern Extended Millimetre Array (NOEMA), having an average flux of $0.55 \mu\text{m}$ at 1.1 mm and $0.03 \mu\text{m}$ at 3 mm. At least for the brightest HELM candidates, follow-ups should

instead be possible with the future NASA Probe far-IR Mission for Astrophysics (PRIMA, P.I. J. Glenn), as has been shown by Bisigello et al. (2025), or with the Atacama Large Millimeter Array (ALMA) for HELM sources in southern fields. Finally, a more in-depth study of these intriguing populations is also pivotal to get a better handle on the main contaminants of ultra-high- z galaxies (Gandolfi et al. 2025; Castellano et al. 2025).

Acknowledgements. The research activities described in this paper were carried out with contribution of the Next Generation EU funds within the National Recovery and Resilience Plan (PNRR), Mission 4 – Education and Research, Component 2 – From Research to Business (M4C2), Investment Line 3.1 – Strengthening and creation of Research Infrastructures, Project IR0000034–“STILES – Strengthening the Italian Leadership in ELT and SKA”. GR, GG and AG are supported by the European Union – NextGenerationEU RFF M4C2 1.1 PRIN 2022 project 2022ZSL4BL INSIGHT. GR and LB acknowledge the support from MIUR gran PRIN 2017 20173ML3WW-0013. GR, LB and MG acknowledge support from INAF under the Large Grant 2022 funding scheme (project “MeerKAT and LOFAR Team up: a Unique Radio Window on Galaxy/AGN co-Evolution”). MG acknowledges support from INAF under the the following funding scheme Large GO 2024 (project “MeerKAT and Euclid Team up: Exploring the galaxy-halo connection at cosmic noon”). LB also acknowledges support from the INAF Large Grant 2022 “Extragalactic Surveys with JWST” (PI Pentericci). This research made use of Photutils, an Astropy package for detection and photometry of astronomical sources (Bradley et al. 2023). This work is based on observations made with the NASA/ESA/CSA James Webb Space Telescope. The data were obtained from the Mikulski Archive for Space Telescopes at the Space Telescope Science Institute, which is operated by the Association of Universities for Research in Astronomy, Inc., under NASA contract NAS 5-03127 for JWST. These observations are associated with program #1345 (doi:10.17909/z7p0-8481).

References

- Alcalde Pampliega, B., Pérez-González, P. G., Barro, G., et al. 2019, *ApJ*, **876**, 135
- Arrabal Haro, P., Dickinson, M., Finkelstein, S. L., et al. 2023a, *ApJ*, **951**, L22
- Arrabal Haro, P., Dickinson, M., Finkelstein, S. L., et al. 2023b, *Nature*, **622**, 707
- Backhaus, B. E., Kirkpatrick, A., Yang, G., et al. 2025, *AJ*, **170**, 300
- Bagley, M. B., Finkelstein, S. L., Koekemoer, A. M., et al. 2023, *ApJ*, **946**, L12
- Barro, G., Pérez-González, P. G., Cava, A., et al. 2019, *ApJS*, **243**, 22
- Barro, G., Pérez-González, P. G., Kocevski, D. D., et al. 2024, *ApJ*, **963**, 128
- Bertin, E., & Arnouts, S. 1996, *A&AS*, **117**, 393
- Bianchi, S., & Schneider, R. 2007, *MNRAS*, **378**, 973
- Bisigello, L., Gandolfi, G., Grazian, A., et al. 2023, *A&A*, **676**, A76
- Bisigello, L., Gandolfi, G., Feltre, A., et al. 2025, *A&A*, **693**, L18
- Bisigello, L., Gruppioni, C., Rodighiero, G., et al. 2025, *J. Astron. Telescopes Instrum. Syst.*, **11**, 031614
- Bocchio, M., Marassi, S., Schneider, R., et al. 2016, *A&A*, **587**, A157
- Bradley, L., Sipőcz, B., Robitaille, T., et al. 2023, <https://doi.org/10.5281/zenodo.7946442>
- Brinchmann, J., Charlot, S., White, S. D. M., et al. 2004, *MNRAS*, **351**, 1151
- Bruzual, G., & Charlot, S. 2003, *MNRAS*, **344**, 1000
- Calzetti, D., Armus, L., Bohlin, R. C., et al. 2000, *ApJ*, **533**, 682
- Carnall, A. C., McLure, R. J., Dunlop, J. S., & Davé, R. 2018, *MNRAS*, **480**, 4379
- Castellano, M., Fontana, A., Merlin, E., et al. 2025, *A&A*, **704**, A158
- Chabrier, G. 2003, *PASP*, **115**, 763
- Dayal, P., Ferrara, A., & Dunlop, J. S. 2013, *MNRAS*, **430**, 2891
- de Graaff, A., Brammer, G., Weibel, A., et al. 2025, *A&A*, **697**, A189
- Draine, B. T. 1990, *ASP Conf. Ser.*, **12**, 193
- Draine, B. T. 2003, *ARA&A*, **41**, 241
- Draine, B. T. 2009, *ASP Conf. Ser.*, **414**, 453
- Duc, P. A., & Mirabel, I. F. 1999, *IAU Symp.*, **186**, 61
- Durodola, E., Pacucci, F., & Hickox, R. C. 2025, *ApJ*, **985**, 169
- Ebrova, I., & Łokas, E. L. 2015, *ApJ*, **813**, 10
- Enia, A., Talia, M., Pozzi, F., et al. 2022, *ApJ*, **927**, 204
- Euclid Collaboration (Bisigello, L., et al.) 2023, *MNRAS*, **520**, 3529
- Euclid Collaboration (Bisigello, L., et al.) 2025, *A&A*, submitted (Euclid Q1 S1), <https://doi.org/10.1051/0004-6361/202554537>
- Finkelstein, S. L., Bagley, M. B., Ferguson, H. C., et al. 2023, *ApJ*, **946**, L13
- Finkelstein, S. L., Leung, G. C. K., Bagley, M. B., et al. 2024, *ApJ*, **969**, L2
- Finkelstein, S. L., Bagley, M. B., Arrabal Haro, P., et al. 2025, *ApJ*, **983**, L4
- Franco, M., Elbaz, D., Béthermin, M., et al. 2018, *A&A*, **620**, A152
- Fudamoto, Y., Oesch, P. A., Schouws, S., et al. 2021, *Nature*, **597**, 489
- Furtak, L. J., Zitrin, A., Plat, A., et al. 2023, *ApJ*, **952**, 142
- Gall, C., Hjorth, J., & Andersen, A. C. 2011, *A&ARv*, **19**, 43
- Gandolfi, G., Rodighiero, G., Bisigello, L., et al. 2025, *A&A*, submitted [arXiv:2502.02637]
- Gentile, F., Talia, M., Behiri, M., et al. 2024, *ApJ*, **962**, 26
- Gentile, F., Talia, M., Enia, A., et al. 2025, *A&A*, **697**, A46
- Gordon, K. D., Clayton, G. C., Misselt, K. A., Landolt, A. U., & Wolff, M. J. 2003, *ApJ*, **594**, 279
- Graziani, L., Schneider, R., Ginolfi, M., et al. 2020, *MNRAS*, **494**, 1071
- Greene, J. E., Labbe, I., Goulding, A. D., et al. 2024, *ApJ*, **964**, 39
- Grogin, N. A., Kocevski, D. D., Faber, S. M., et al. 2011, *ApJS*, **197**, 35
- Gruppioni, C., Béthermin, M., Loiacono, F., et al. 2020, *A&A*, **643**, A8
- Harikane, Y., Zhang, Y., Nakajima, K., et al. 2023, *ApJ*, **959**, 39
- Holwerda, B. W., Hsu, C.-C., Hathi, N., et al. 2024, *MNRAS*, **529**, 1067
- Killi, M., Watson, D., Brammer, G., et al. 2024, *A&A*, **691**, A52
- Kocevski, D. D., Onoue, M., Inayoshi, K., et al. 2023, *ApJ*, **954**, L4
- Kocevski, D. D., Finkelstein, S. L., Barro, G., et al. 2025, *ApJ*, **986**, 126
- Koekemoer, A. M., Faber, S. M., Ferguson, H. C., et al. 2011, *ApJS*, **197**, 36
- Labbe, I., Greene, J. E., Matthee, J., et al. 2024, *ApJ*, submitted [arXiv:2412.04557]
- Labbe, I., Greene, J. E., Bezanson, R., et al. 2025, *ApJ*, **978**, 92
- Lelli, F., Duc, P.-A., Brinks, E., et al. 2015, *A&A*, **584**, A113
- Li, H., Mao, S., Emsellem, E., et al. 2018, *MNRAS*, **473**, 1489
- Liu, Z., Morishita, T., & Kodama, T. 2024, *ApJ*, submitted [arXiv:2406.11188]
- Llerena, M., Amorín, R., Pentericci, L., et al. 2024, *A&A*, **691**, A59
- Ma, Y., Greene, J. E., Setton, D. J., et al. 2025, *ApJ*, submitted [arXiv:2504.08032]
- Magnelli, B., Adscheid, S., Wang, T.-M., et al. 2024, *A&A*, **688**, A55
- Mancini, M., Schneider, R., Graziani, L., et al. 2015, *MNRAS*, **451**, L70
- Matthee, J., Naidu, R. P., Brammer, G., et al. 2024, *ApJ*, **963**, 129
- McLure, R. J., Dunlop, J. S., Cullen, F., et al. 2018, *MNRAS*, **476**, 3991
- Mérida, R. M., Pérez-González, P. G., Sánchez-Blázquez, P., et al. 2023, *ApJ*, **950**, 125
- Nanayakkara, T., Glazebrook, K., Schreiber, C., et al. 2025, *ApJ*, **981**, 78
- Noeske, K. G., Weiner, B. J., Faber, S. M., et al. 2007, *ApJ*, **660**, L43
- Nozawa, T., Maeda, K., Kozasa, T., et al. 2011, *ApJ*, **736**, 45
- Oke, J. B., & Gunn, J. E. 1983, *ApJ*, **266**, 713
- Pandya, V., Zhang, H., Huertas-Company, M., et al. 2024, *ApJ*, **963**, 54
- Pannella, M., Elbaz, D., Daddi, E., et al. 2015, *ApJ*, **807**, 141
- Peng, C. Y., Ho, L. C., Impey, C. D., & Rix, H.-W. 2010, *AJ*, **139**, 2097
- Pérez-González, P. G., Rieke, G. H., Egami, E., et al. 2005, *ApJ*, **630**, 82
- Pérez-González, P. G., Rieke, G. H., Villar, V., et al. 2008, *ApJ*, **675**, 234
- Pérez-González, P. G., Barro, G., Annunziatella, M., et al. 2023, *ApJ*, **946**, L16
- Pérez-González, P. G., Barro, G., Rieke, G. H., et al. 2024, *ApJ*, **968**, 4
- Pérez-González, P. G., Östlin, G., Costantin, L., et al. 2025, *ApJ*, **991**, 179
- Pirzkal, N., Rothberg, B., Ryan, R. E., et al. 2018, *ApJ*, **868**, 61
- Popping, G., Somerville, R. S., & Galametz, M. 2017, *MNRAS*, **471**, 3152
- Rodighiero, G., Vaccari, M., Franceschini, A., et al. 2010, *A&A*, **515**, A8
- Rodighiero, G., Bisigello, L., Iani, E., et al. 2023, *MNRAS*, **518**, L19
- Salim, S., & Narayanan, D. 2020, *ARA&A*, **58**, 529
- Sarang, A., Matsuura, M., & Micelotta, E. R. 2018, *Space Sci. Rev.*, **214**, 63
- Schneider, R., & Maiolino, R. 2024, *A&ARv*, **32**, 2
- Schneider, R., Hunt, L., & Valiante, R. 2016, *MNRAS*, **457**, 1842
- Shapley, A. E., Sanders, R. L., Reddy, N. A., Topping, M. W., & Brammer, G. B. 2023, *ApJ*, **954**, 157
- Simpson, J. M., Swinbank, A. M., Smail, I., et al. 2014, *ApJ*, **788**, 125
- Talia, M., Cimatti, A., Giuliotti, M., et al. 2021, *ApJ*, **909**, 23
- Taylor, A. J., Finkelstein, S. L., Kocevski, D. D., et al. 2025, *ApJ*, **986**, 165
- Traina, A., Gruppioni, C., Delvecchio, I., et al. 2026, *A&A*, **705**, A255
- Tsatsi, A., Lyubenova, M., van de Ven, G., et al. 2017, *A&A*, **606**, A62
- Wang, T., Schreiber, C., Elbaz, D., et al. 2019, *Nature*, **572**, 211
- Williams, C. C., Alberts, S., Ji, Z., et al. 2024, *ApJ*, **968**, 34
- Yang, G., Papovich, C., Bagley, M. B., et al. 2023, *ApJ*, **956**, L12
- Zavala, J. A., Aretxaga, I., Geach, J. E., et al. 2017, *MNRAS*, **464**, 3369
- Zavala, J. A., Buat, V., Casey, C. M., et al. 2023, *ApJ*, **943**, L9
- Zwicky, F. 1956, *Ergebnisse der exakten Naturwissenschaften*, **29**, 344

Appendix A: Comparison between different SED fitting runs

In this Appendix we report on the comparison between the stellar mass and redshift derived with the different SED fitting configurations (see Sec. 2.2) for the three HELM samples. The comparison is shown in Fig. A.1.

On average, the delayed SFH produces the lowest stellar mass, while the double power-law SFH produces the highest, but the average difference remains below 0.09 dex. On the contrary, the double power-law SFH corresponds to the smallest redshift, while the delayed SFH with the SMC reddening laws results in the highest one. Also in this case the differences are negligible (i.e. $\Delta z < 0.09$).

It is worth noticing that in the case of the HELM-1 σ sample there are some solutions with $z > 7$. This happens for 2 objects with the double power-law SFH.

Appendix B: Visual inspection

In Figures B.1 and B.2 we reported, as example, the cut-outs of the sources in the HELM-3 σ and HELM-2 σ that we removed after visual inspection. We do not report the cut-outs for the HELM-1 σ given the size of the sample. As visible in the Figures, there are different reasons that motivate our choice to remove these sources. In some cases no source is visible at the expected position, while in other cases the source has a strange shape which sometimes varies between filters. In other, more simple cases, the source is simply outside the field of view of some NIR-Cam filters.

Appendix C: Available spectroscopic data

As mentioned in Section 2.3, we matched our photometrically selected samples with the available spectroscopic data to remove possible contaminants or validate HELM sources. This step was performed before creating the final HELM samples and we discussed in this Section the analysed sources. Spectroscopic data is available as part of the CEERS survey and from the DAWN JWST Archive. The first spectroscopic data consist of slitless NIRCam WFSS spectra (N. Pirzkal, private communication; see Pirzkal et al. 2018, for grism data reduction details) and NIRSPEC MSA PRISM and medium resolution spectra taken as part of programme DD-2750 (P.I. Arrabal Haro Arrabal Haro et al. 2023b). Given the faintness of our sample, we do not expect many galaxies to be present in the NIRCam WFSS sample, which includes only galaxies with $F356W \leq 25$ mag. Indeed, only three HELM candidates, which are in the HELM-1 σ sample, have slitless spectra, but the signal-to-noise ratio is so low that neither spectral lines nor continuum features are detectable.

There are instead ten objects that have NIRSpec PRISM data, one in the HELM-3 σ sample, one in the HELM-2 σ sample, and eight in the HELM-1 σ . From the DJA we retrieved other eight NIRSpec spectra, seven from the Red Unknowns: Bright Infrared Extragalactic Survey (RUBIES; de Graaff et al. 2025) and one from the Cycle 1 GO-2565 (P.I. K. Glazebrook), which however is not among the massive quiescent galaxies described by Nanayakkara et al. (2025). Of these sources, seven are in the HELM-1 σ sample and one is in the HELM-2 σ one. Overall, we have spectroscopic data for one HELM-3 σ source that was rejected, two HELM-2 σ sources, one of which was confirmed while the other was rejected, and eleven HELM-1 σ sources, nine of which were rejected, while the data were not discriminating

enough for two galaxies. We discuss them in more detail in the rest of this section.

C.1. HELM-3 σ spectrum

Figure C.1 shows the only object in the HELM-3 σ sample with spectroscopic data, which is CEERS-71266. As visible, there are no evident line emissions, suggesting moderate star formation, but the stellar continuum is visible at $\lambda > 1.4 \mu\text{m}$. There are some faint absorption features, which combined with the visible continuum break suggest that the galaxy may be located at $z = 2.35$. While more data are necessary to more robustly validate this possibility, when performing a photometric fit with BAGPIPES, using a set-up similar to the one in Section 2.2 with a delayed SFHs and fixing the redshift to $z = 2.35$, we obtained a stellar mass of $\log_{10}(M_*/M_\odot) = 9.3 \pm 0.1$ and a dust attenuation of $A_V = 0.4 \pm 0.2$ mag. Given that this galaxy is outside the HELM selection we removed it from the final HELM sample.

C.2. HELM-2 σ spectra

There are two sources with spectroscopic data that were originally in the HELM-2 σ sample, one of them has been confirmed, while the other is a contaminant.

CEERS-14821

The first source we discuss in the -2 σ sample is CEERS-14821, which has been observed as part of the Director's Discretionary Time programme JWST-DDT 2750 (PI Arrabal Haro; Arrabal Haro et al. 2023b) and has been presented in detail in Bisigello et al. (2025). The object has a spectroscopic redshift of $z_{\text{spec}} = 4.883 \pm 0.003$ based on the [O III]5007Å line, which is the brightest. The H_α , H_β , H_γ and [O III]4959Å nebular emission lines are also detected. A careful spectro-photometric fit of the available data is presented in Bisigello et al. (2025) and confirms the HELM nature of this source, which has $A_V = 2.2^{+0.5}_{-0.6}$ mag, considering the reddening law by Calzetti et al. (2000), and a stellar mass of $\log_{10}(M_*/M_\odot) = 8.17^{+0.05}_{-0.04}$.

CEERS-14821 is at very high- z with respect to the rest of the HELM population, so it may be not representative of the entire population. It however advocates on the necessity of spectroscopic follow-ups, to verify the nature and properties of these intriguing sources.

CEERS-46775

The second galaxy in the HELM-2 σ sample with spectroscopic data is CEERS-46775. This galaxy has been observed as part of the RUBIES survey with the G395M/F290LP grating and filter. This source has a spectroscopic redshift of $z = 4.81353 \pm 0.00008$ derived from the [O III]5007Å and H_α emission lines (Fig. C.2). The [O III]4959Å is at the edge of the spectrum, while H_β is outside the wavelength coverage, preventing us from measuring the dust extinction directly from the Balmer decrement. We performed a spectro-photometric fit with bagpipes, fixing the redshift to the spectroscopic one and considering a non parametric SFH. We this set-up, we derived a stellar mass of $\log_{10}(M_*/M_\odot) = 9.13^{+0.25}_{-0.04}$ and a dust attenuation of $A_V = 0.03^{+0.05}_{-0.2}$ mag, completely outside the HELM selection. We therefore remove this object from the HELM-2 σ sample.

C.3. HELM-1 σ spectra

Eleven sources originally present in the HELM-1 σ have NIR-Spec spectroscopic data. None of them were confirmed as HELM sources.

CEERS-45809

This object was part of the HELM-1 σ sample, has visible H_β and [O III]5007Å lines (Fig. C.3, first panel) and is inside the sample of extreme line emitters by Llerena et al. (2024). The spectroscopic redshift is $z_{spec} = 7.49$, but given that a single Hydrogen line is visible, it is not possible to derive the dust attenuation from the spectrum. We performed a spectro-photometric fit using BAGPIPES and a set-up similar to the one presented in Section 2.2, but considering a non-parametric SFH which is possible given that the spectroscopic redshift is available, as done by Bisigello et al. (2025). From the fit we derived a stellar mass of $\log_{10}(M_*/M_\odot) = 7.94^{+0.14}_{-0.09}$ and a dust attenuation $A_V = 0.9^{+0.1}_{-0.1}$ mag, so this galaxy is just outside the HELM definition defined in eq. 1 and we removed it from the final sample.

CEERS-45766

The NIRSpec PRISM spectrum of CEERS-45766, which is shown in Fig. C.3 (second row), shows a tentative detection of a single line, which is not sufficient to derive a robust spectroscopic redshift. In particular, the line is located at $\lambda = 3.3 \mu\text{m}$ with an observed flux of $(2.66 \pm 0.32) \times 10^{-19}$ erg/s/cm², but there are no other robust lines. If the visible line is H_α , the galaxy should be at $z = 4.0$, while if the line is the [O III]5007 Å nebular line, the galaxy should be at $z = 5.6$. In the first case, the noise is too high to derive any stringent lower limit in the dust attenuation from the non detection of H_β . In the second case, we would expect to observe H_α at $\lambda = 4.33 \mu\text{m}$, but nothing is visible in that part of the spectrum, which is however quite noisy. Another possibility is that the line is Pa α at a $z = 0.76$, which would be consistent with the photometric redshift that ranges from $z = 0.2$ to $z = 1.4$, depending on the SED fitting set-up. In this case we would expect to observe the H_α line at $1.15 \mu\text{m}$, if the galaxy does not have an extreme dust attenuation, but no lines are visible in that area of the spectrum.

If we repeat the SED fitting described in Section 2.2, but fixing to one of the possible redshifts, we retrieved a dwarf galaxy $\log_{10}(M_*/M_\odot) \sim 8.0$, but not a dusty one as $A_V = 0.3 \pm 0.2$ mag for the $z \geq 4$ solutions. If instead we fixed the the redshift to $z = 0.76$ we retrieved a less massive galaxy $\log_{10}(M_*/M_\odot) \sim 7.2$ with $A_V = 1 \pm 0.5$ mag, which is however not enough to justify the completely absorb the H_α line. Considering these results, we decided to remove this source from the HELM-1 σ sample.

CEERS-29979

This spectrum was obtained from the Cycle 1 GO-2565 program (P.I. K. Glazebrook). We derived a spectroscopic redshift of $z = 3.788 \pm 0.004$ from the [O III]5007Å emission line. While the H_α line is also visible in the spectrum (Fig. C.3), the H_β line is not detected. Given the spectrum's low S/N ratio, we proceeded by performing the SED fit at a fixed spectroscopic redshift, including only the photometric data. From this fit, we derived a stellar mass of $\log_{10}(M_*/M_\odot) = 8.1^{+0.1}_{-0.1}$ and $A_V = 0.5^{+0.1}_{-0.1}$, placing this

galaxy outside the HELM selection. We therefore remove this source from the sample.

CEERS-30063

CEERS-30063 has been observed as part of the RUBIES survey with the medium resolution PRISM/CLEAR and G395M/F290LP disperser-filter combinations, but the latter is too noisy to identify any feature. The spectroscopic redshift is $z = 5.307 \pm 0.006$ derived from the [O III]5007Å line. The H_α is also visible, but the S/N is quite limited (Fig. C.3) preventing us to derive the dust attenuation directly from the spectrum. We performed a spectro-photometric fit, including only the part of spectrum around fluxes with S/N > 3. From the fit we derive a stellar mass of $\log_{10}(M_*/M_\odot) = 8.4^{+0.1}_{-0.1}$ and $A_V = 0.2^{+0.2}_{-0.2}$, which move this galaxy outside the HELM selection.

CEERS-19613

CEERS-19613 has been observed as part of the RUBIES survey with the PRISM/CLEAR and G395M/F290LP disperser-filter combinations. The spectroscopic redshift is $z = 5.9828 \pm 0.0001$ derived from the [O III]5007Å line in the highest resolution spectrum, but many other nebular line are visible, among with both H_α and H_β . From their ratio in the G395M/F290LP spectrum, we derived that the dust attenuation is $A_V = 3.4^{+1.0}_{-0.9}$ using the Calzetti et al. (2000) reddening law, but it remains large ($A_V = 2.5^{+0.8}_{-1.1}$) even considering the maximum contribution from the stellar absorption below the H_β line. We performed a spectro-photometric fit, fixing the redshift to the spectroscopic value, allowing the dust-extinction to varies between the 1 σ uncertainties derived from the spectrum and considering a non parametric SFH. We obtained a stellar mass of $\log_{10}(M_*/M_\odot) = 9.6^{+0.1}_{-0.1}$, which would place this galaxy just outside the HELM selection. However the code struggle to fit the data hitting the upper boundary for the ionisation parameter. We remove this source from the HELM sample.

CEERS-65042

This source has been observed as part of the RUBIES survey only with the G395M/F290L configuration. It has a spectroscopic redshift of $z = 7.0332 \pm 0.0005$ derived from the [O III]5007Å. In the spectrum it is visible a faint H_β line, while the H_α is outside the wavelength range covered. We perform a spectro-photometric fit with non-parametric SFH obtaining a stellar mass of $\log_{10}(M_*/M_\odot) = 8.9^{+0.1}_{-0.2}$ and a dust attenuation of $A_V = 1.1^{+0.1}_{-0.2}$, which move this object slightly outside the HELM selection.

CEERS-73265

This source has been observed as part of the RUBIES survey with the PRISM/CLEAR and the G395M/F290L configurations. However, the first one is affected by contamination issues, while the spectra of the second is affected by artefacts only at long wavelengths. We obtain a redshift of $z = 7.793 \pm 0.001$ from the [O III]5007Å, but only the [O III]5007 doublet is clearly visible. We perform a spectro-photometric fit with non-parametric SFH obtaining a stellar mass of $\log_{10}(M_*/M_\odot) = 8.7^{+0.1}_{-0.2}$ and a dust attenuation of $A_V = 0.5^{+0.2}_{-0.2}$, which move this object outside the HELM selection.

CEERS-81024

This source has been observed as part of the RUBIES survey only with the PRISM/CLEAR configuration. It has a spectroscopic redshift of $z = 7.189 \pm 0.002$ derived from the [O III]5007Å and only the [O III]5007 doublet is clearly visible. We perform a spectro-photometric fit with non-parametric SFH obtaining a stellar mass of $\log_{10}(M_*/M_\odot) = 8.8^{+0.2}_{-0.2}$ and a dust attenuation of $A_V = 0.6^{+0.1}_{-0.2}$, which move this object outside the HELM selection.

CEERS-45630

This source has been observed as part of the RUBIES survey with the PRISM/CLEAR configuration. Only a single line is visible in the spectrum and if it corresponds to the [O III]5007Å line it would place the galaxy at $z = 8.772 \pm 0.002$. We perform a spectro-photometric fit with non-parametric SFH obtaining a stellar mass of $\log_{10}(M_*/M_\odot) = 8.3^{+0.3}_{-0.2}$ and a dust attenuation of $A_V = 0.6^{+0.1}_{-0.2}$, which move this object outside the HELM selection.

CEERS-87502, CEERS-19610

The NIRSpc PRISM spectra of CEERS-87502 and CEERS-19610, which are shown in Fig. C.3 (third and fourth rows), show no evident nebular emission lines nor stellar continuum, so no conclusive statements can be made on the nature of these objects.

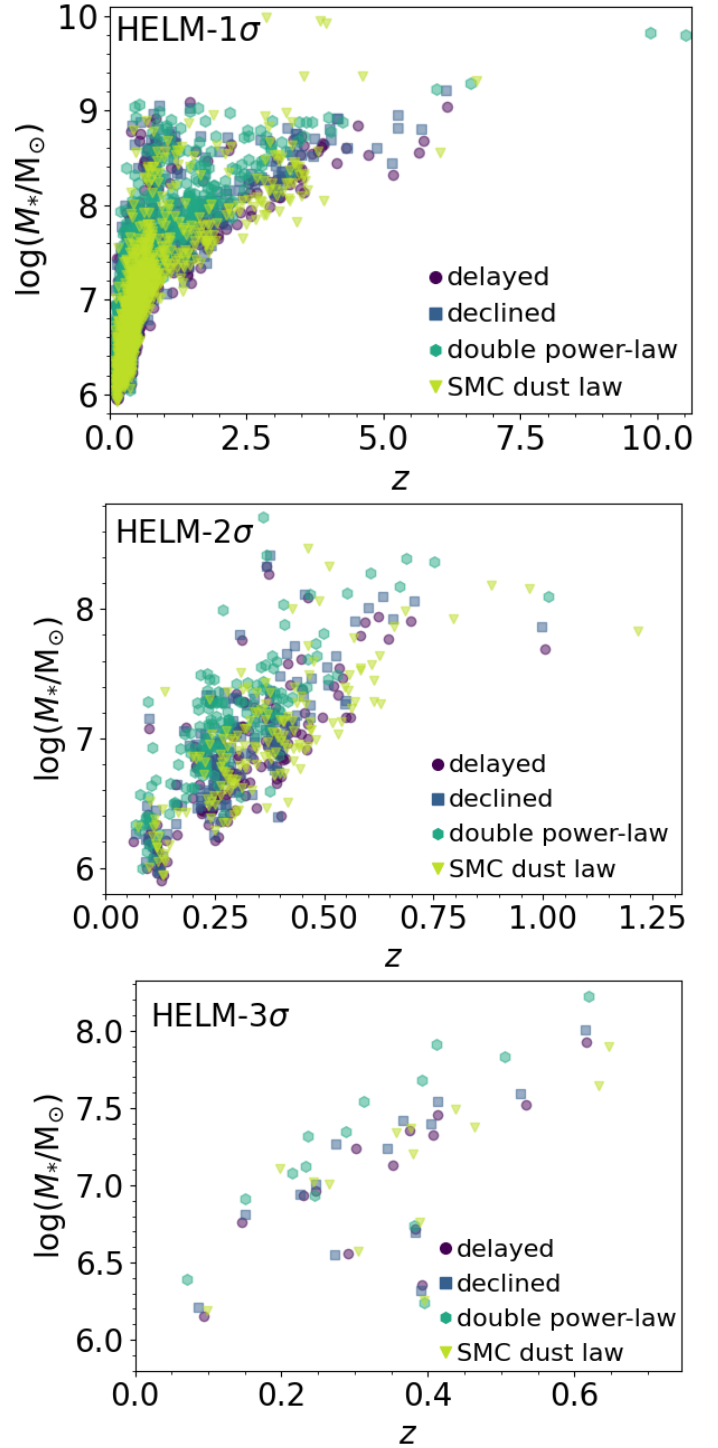


Fig. A.1. Comparison between the redshift and the stellar mass obtained with the different SED runs. The comparison is performed for the HELM-1 σ (top), the HELM-2 σ (centre), and the HELM-3 σ samples. Different colours indicate different SED fitting configurations: delayed SFH (pink circles), declined SFH (grey squares), double power-law SFH (olive hexagons), and delayed SFH with SMC dust attenuation law (cyan triangles). For the HELM-2 σ we did not show, for clarity, three data points at $z = 4.5$ and $z = 10.6$, obtained with the delayed SFH with both reddening laws and the double power-law SFH, respectively.

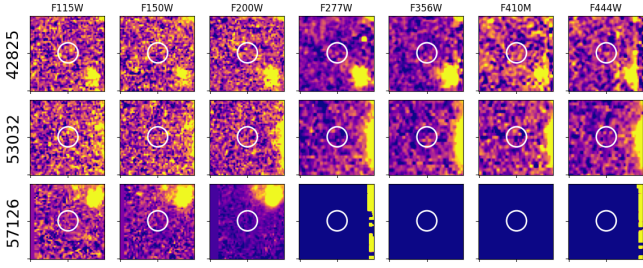


Fig. B.1. NIRCcam cut-outs of the three HELM- 3σ sources removed after visual inspection. Each cut-out is $1''.5 \times 1''.5$ and the white circle indicates the position of the source.

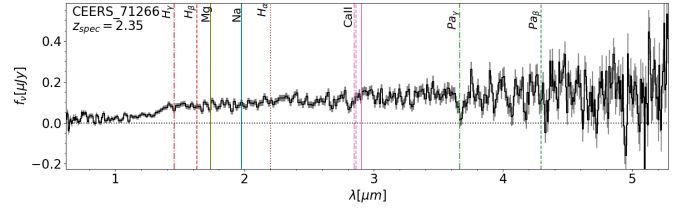


Fig. C.1. The only source in the HELM- 3σ sample with NIRSpc spectroscopic data. No emission lines are clearly visible, while there are some possible absorption features.

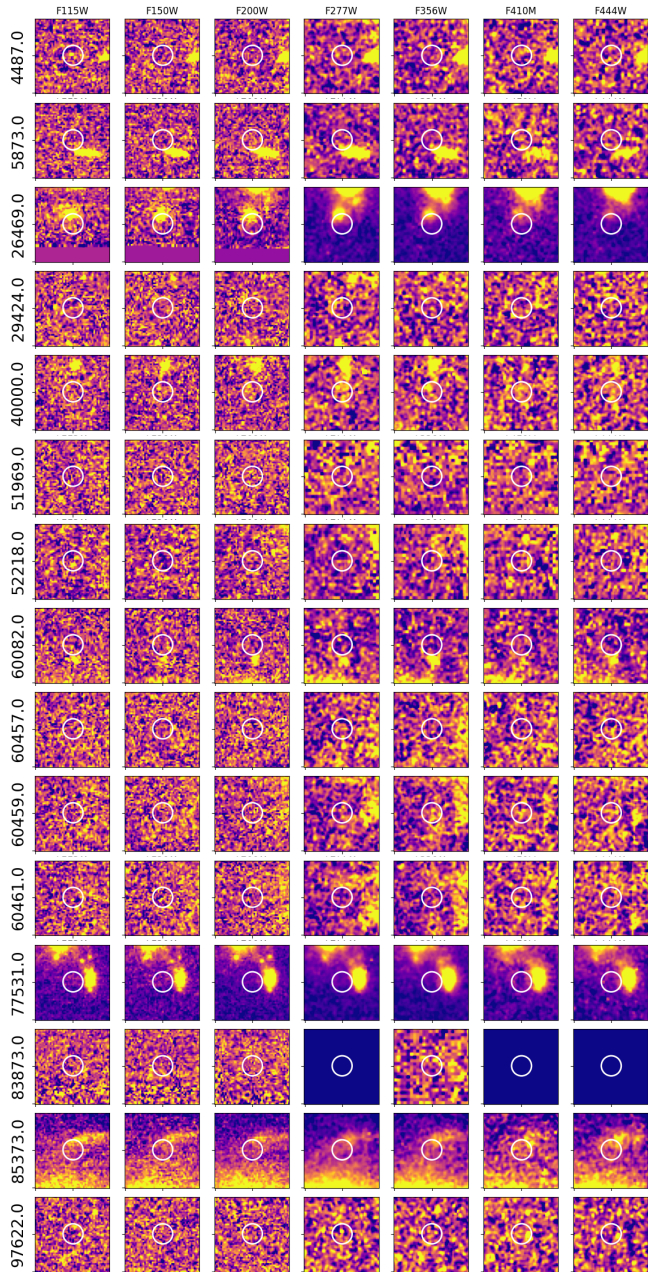


Fig. B.2. NIRCcam cut-outs of the fifteen HELM- 2σ sources removed after visual inspection. Each cut-out is $1''.5 \times 1''.5$ and the white circle indicates the position of the source.

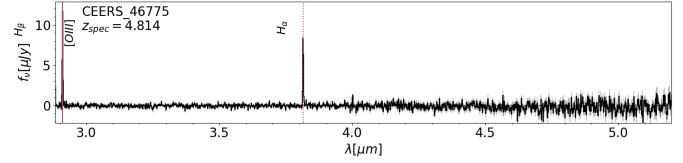


Fig. C.2. CEERS-45766, a source in the HELM- 2σ sample with medium resolution (G395M) NIRSpc data. The other source in the HELM- 2σ catalog was presented in Bisigello et al. (2023).

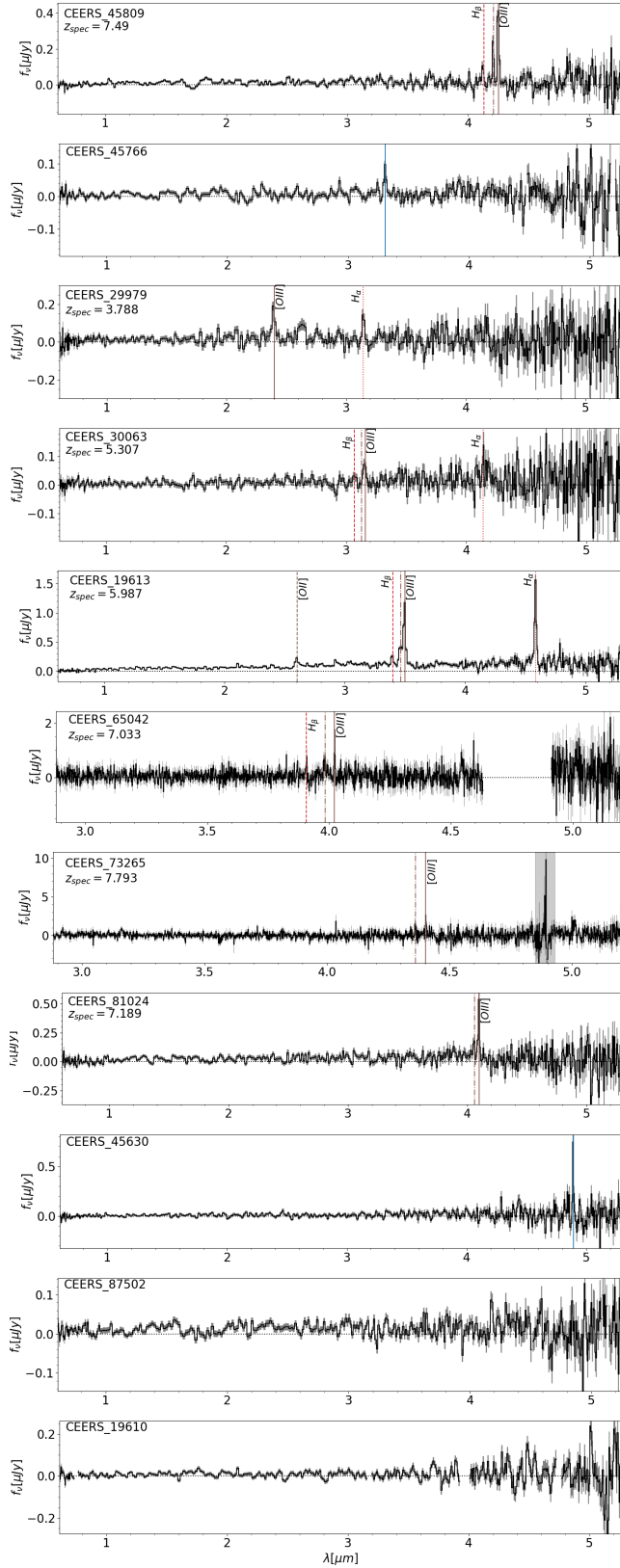


Fig. C.3. Sources in the HELM-1 σ sample with NIRSPEC spectroscopic data. Vertical lines show nebular emission lines present in the spectra. In two objects (CEERS-45766 and CEERS-45630), only one emission line is visible preventing us to securely identify it. Other two spectra (CEERS-87502 and CEERS-19610) show no evident features. In the top left of each panel we report the source identification number and the derived spectroscopic redshift, if available.